Available online at www.sciencedirect.com
ScienceDirect
Journal of Computational Physics 223 (2007) 519–550
JOURNAL OF COMPUTATIONAL PHYSICS
www.elsevier.com/locate/jcp

An efficient algorithm for scalar PDF modelling in incompressible turbulent flow; numerical analysis with evaluation of IEM and IECM micro-mixing models

M. Cassiani [a,*], A. Radicchi [b], J.D. Albertson [a], U. Giostra [b]

[a] *Department of Civil and Environmental Engineering, Duke University, Durham, NC 27708, USA*
[b] *Facoltà di Scienze Ambientali, Università degli studi di Urbino "Carlo Bo", 61029 Urbino, Italy*

Received 26 April 2006; received in revised form 19 September 2006; accepted 21 September 2006
Available online 28 November 2006

Abstract

In this paper, we investigate the application of probability density function (PDF) Monte Carlo methods to scalar release from small sources in a turbulent flow spanning a large physical domain. This is a typical situation encountered when modeling the dispersion of a gaseous substance in the atmosphere. Monte Carlo PDF methods have recently been applied to atmospheric modeling responding to the need for predicting the higher statistics and the concentration PDF generated by the continuous release of reactive and non-reactive substances. In this work we introduce some optimized numerical techniques based on the paradigm that the main field of interest is the scalar field and not the fluid dynamic field; the scalar are considered dynamically passive and the statistical characteristics of the turbulence velocity field are assumed known. These techniques are a block-structured grid coupled with a particle splitting/erasing algorithm and a localized time stepping. The proposed technique is different from others presented before since the particle splitting and erasing is done in a more straightforward and consistent manner. This method has been applied to the study of scalar dispersion from localized line sources in a canopy generated boundary layer. The line source has been treated as a point source in a two-dimensional space but the extension to three dimensions is straightforward. Our framework allows for an evaluation of the effects induced by different levels of discretization in the velocity space of the involved micro-mixing model, starting from the interaction by the exchange with the mean (IEM) toward the more physically consistent interaction by exchange with the conditional mean (IECM). Therefore, aside from the algorithm description and a complete numerical analysis of the code, a comparison between the IEM and IECM micro-mixing models has been investigated.

Keywords: Incompressible flows; Turbulent flows; Scalar dispersion; Mixing; Probability density function; Monte Carlo method; Particle method; Numerical analysis

* Corresponding author. Tel.: +1 919 668 3809.
E-mail address: mcassian@duke.edu (M. Cassiani).

0021-9991/$ - see front matter © 2006 Elsevier Inc. All rights reserved.
doi:10.1016/j.jcp.2006.09.023

Nomenclature

a_i	drift coefficient
b_{ij}	diffusion coefficient
B_{ij}	$b_{ij}b_{jk}/2$
B_Q	bias
b_Q	bias coefficient
C_0	Kolmogorov constant for the Lagrangian velocity structure function
C_r	Richardson–Obhukov constant
C_ϕ	micro-mixing constant
d_r	relative expansion
D_Q	discretization error
$\mathscr{D}_Q$	deterministic error for Q
e	turbulent kinetic energy
$\mathscr{E}_Q$	computational error for Q
$f_{\phi U}$	velocity-composition joint PDF
f_u^*	modelled fluctuating velocity PDF
f_ϕ^*	modelled fluctuating composition PDF
$f_{\phi u}^*$	modelled fluctuating velocity-composition joint PDF
f_L	Lagrangian PDF
g_i	gravitational acceleration vector
i_c	cell index
$\widehat{\mathscr{K}}$	kernel function
l	subgrid index
L	length scale of most energetic eddies
L_x, L_y	domain dimensions
m	computational weight
n	particle splitting factor
N_b	number of subgrids
N_c	total cell number
N_p	total number of particles
$N_\mathrm{p}^{(i_\mathrm{c})}$	number of particles in cell i_c
N_{u_i}	number of velocity cells in u_i space
Q	generic quantity
$\mathscr{Q}$	source emission factor
q_1	probability for a particle to survive in SE algorithm
q_2	probability for a particle to be erased in SE algorithm
$\langle p \rangle$	mean pressure
p'	fluctuating pressure
r_Q	autocorrelation function of the process Q
$\mathscr{R}_Q$	variance reduction factor for time averaging
$\mathscr{S}_Q$	statistical error for Q
S_α	αth scalar source/reaction term
t	time variable
$t_\mathrm{s}^{(\mathrm{adim})}$	adimensional calculation time for each time step
$t_Q^{(\mathrm{c})}$	Q signal correlation time
T_L	Lagrangian integral time scale
T_av	averaging time
T_s	time to reach stationarity
T_j	local particle age

$T_j^{(r)}$	local residence time of particle j in every cell
U_i	velocity
V_i	sample space for velocity
u_i	fluctuating velocity
v_i	sample space for fluctuating velocity
U	horizontal component of velocity
V	vertical component of velocity
u	horizontal component of fluctuating velocity
v	vertical component of fluctuating velocity
u_i^*	modelled fluctuating velocity
$\langle U_i \rangle$	mean velocity
x_i	ith spatial coordinate
x_i^*	modelled position
y_{i0}	initial particle position
$\langle y \rangle$	mean plume height
$\boldsymbol{Z}$	state vector of (x_i, u_i, ϕ_α) process
$\boldsymbol{z}$	sample space of $\boldsymbol{Z}$
α_Q	statistical error slope
$\alpha^{(\mathrm{loc})}$	local time coefficient
$\alpha^{(\mathrm{g})}$	global time coefficient
δ	Dirac delta
δ_{ij}	Kronecker delta
$\Delta t^{(\mathrm{g})}$	global time step
$\Delta t^{(\mathrm{loc})}$	local particle time step
$\Delta x, \Delta y$	cell dimensions
γ	velocity space transformation angle
$\Gamma_{(\alpha)}$	molecular diffusion of α
ε	dissipation rate of turbulent kinetic energy
τ	turbulence time scale
τ_{ij}	Reynolds stress tensor
τ_{L}	Lagrangian integral time scale
τ_{m}	micro-mixing time scale
τ_ϕ	dissipation time scale of concentration variance
Θ_i	variable for drift coefficient definition
ϑ	standardized random variable
ϕ_α	composition variable for α
ϕ_α^*	modelled random variable for α particle composition
$\phi_{\mathrm{s}}(x, y)$	source composition
φ_α	micro-mixing term for αth scalar species
ψ_α	sample space variable for αth scalar species
ρ	density of fluid (air)
μ_x, μ_y	scalar source coordinates
ν	kinematic viscosity
σ	locally averaged velocity variance
σ_0	scalar source size
σ_y	mean plume depth
σ_{r}	instantaneous plume spread
σ_{u_i}	u_i standard deviation
σ_{ur}	relative velocity fluctuation
σ_ϕ	standard deviation of ϕ
σ_ξ, σ_η	standard deviation of transformed fluctuating velocities

λ_{ij}	inverse of Reynolds stress tensor
ξ, η	transformed fluctuating velocities
ζ_j	Wiener process
$\langle \cdot \rangle$	ensemble average
$\langle \cdot \mid \cdot \rangle$	conditional ensemble average
$\widetilde{\cdot}$	cell average
$\bar{\cdot}$	time average
$[\cdot]_R$	relative error

1. Introduction

The probability density function (PDF)/Monte Carlo method is a useful technique for chemical engineering applications, and more in general in such disciplines where complex turbulent reactive flows are studied [10,24,26]. This is the case, for example, of atmospheric dispersion modelling, where the behavior of many reactive species in high Reynolds number turbulent flows has to be predicted. Nevertheless the application to the atmospheric dispersion problem has been investigated only recently [2,14,17].

In general, the strength of the PDF approach lies in the ability to deal exactly with chemical reactions and to reproduce all one-point statistical properties (i.e., one-point PDF) of the related concentration field. This means that unclosed terms do not arise in the equation due to chemical reaction.

Here, we use a velocity-composition joint PDF approach in which the one-point statistics of both velocity and concentration are considered. In the standard method [26,29] both the PDF of velocity and that of concentration are considered unknown. Here we modify this method by coupling the Thomson's [40] approach for the motion of fluid particles with a standard PDF technique for the concentration. In other words, we are actually using an assumed shape for the velocity PDF while we are dealing with an unknown PDF of the concentration. This kind of coupling has shown to be very powerful when the turbulence structure is sufficiently predictable and main flow statistics are available from measurements [2–5].

In the Lagrangian PDF/Monte Carlo approach a large number of particles are moved in the computational domain while solving a system of stochastic differential equations (SDEs) for position, velocity and concentration carried by each particle. By some sort of grid-averaging procedure we obtain a discretized velocity-composition joint PDF which represents the solution of the studied problem. To obtain meaningful solutions an adequate number of particles must be used in the averaging.

In many practical cases the computational requirements of PDF technique can become very high due to the dimensionality of the problem, the number of the chemical species involved and the need to adequately resolve inhomogeneity in the flow and/or scalar fields. In such a case optimized computational techniques have to be applied. Some studies have been devoted to this topic (see e.g. [18,15,22,31]).

The use of an assumed velocity PDF to move particles in a turbulent flow is a standard procedure in atmospheric application (see e.g. [42]) and allows us to introduce a PDF/Monte Carlo algorithm specifically optimized for the efficient computation of the properties of the scalars field. We note that the sources size of scalars emitted in the atmosphere is usually very small compared to the size of the domain interested by the dispersion thus imposing severe limitations to the applicability of non-optimized PDF methods.

In the present work we model the dispersion of a dynamically passive (i.e., not altering the flow field) non-reacting scalar released from a small and localized (point) source in a two-dimensional space; this can be considered as a prototype of real world applications. In the region close to the source a high level of detail is required while in zones away from the source coarser grid can be used. For this purpose a non-homogeneous block-structured grid is employed and coupled with a particle splitting and erasing technique. These techniques are useful for the reduction of computational errors in smaller cells and more generally for the optimization of the particle distribution/localization within the computational domain. We note that the use of an unstructured grid would be also possible but an unstructured grid requires more expensive computational procedure to locate particles and does not allow an efficient treatment of the particle splitting and erasing. For example in [18] a mass sorting algorithm was used in each cell before application of the particle splitting and erasing. With a block-structured grid this is not needed, and the correct particles density is maintained in a straightforward manner as we will see in detail in Section 3. Moreover, in the application related to atmo-

spheric scalar dispersion there is no need of the extra flexibility allowed by unstructured grid that, on the contrary, can be fundamental when fluid dynamic calculations are involved.

A complete numerical analysis of the algorithm is performed following the work of [43] to accurately evaluate the effects of the block-structured grid and particle splitting and erasing technique. Besides the numerical analysis a comparison is performed between discretized versions of two micro-mixing models: interaction by exchange with the mean (IEM) and interaction by exchange with the conditional (over the velocity) mean (IECM). We point out that from a discretized point of view the IEM could actually be viewed as a IECM model with only one velocity class. A micro-mixing model represents a fundamental part of composition PDF modeling because it simulates the dissipative effects of scalar fluctuation associated with turbulence and molecular diffusivity. What will appear from the analysis is that even a small increase in the number of velocity classes used (from one to three) gives a great improvement in the model results.

In the next section the PDF transport equation is introduced and the relationships with a system of SDEs are discussed. Section 3 introduces the numerical algorithm. The numerical analysis is conducted in Section 4.

2. PDF approach

This section introduces the fundamental concepts of the PDF modelling applied to turbulent dispersion.

2.1. Basic equations

The exact transport equation for the *one-point* joint velocity-composition PDF, $f_{\phi U} \equiv f(t, x_i, V_i, \psi_\alpha)$, of an incompressible fluid is

$$\frac{\partial f_{\phi U}}{\partial t} + V_i \frac{\partial f_{\phi U}}{\partial x_i} + \left(g_i - \frac{1}{\rho} \frac{\partial \langle p \rangle}{\partial x_i} \right) \frac{\partial f_{\phi U}}{\partial V_i} + \frac{\partial}{\partial \psi_\alpha} [f_{\phi U} S_\alpha(\boldsymbol{\psi})] = -\frac{\partial}{\partial V_i} \left(f_{\phi U} \left\langle \nu \nabla^2 U_i - \frac{1}{\rho} \frac{\partial p'}{\partial x_i} | \boldsymbol{Z} = \boldsymbol{z} \right\rangle \right) - \frac{\partial}{\partial \psi_\alpha} \left(f_{\phi U} \langle \Gamma_{(\alpha)} \nabla^2 \phi_\alpha | \boldsymbol{Z} = \boldsymbol{z} \rangle \right), \tag{1}$$

and can be obtained with standard methods from the Navier–Stokes equation and the scalar transport equation (see [29]). In this equation x_i represents the physical space variable, U_i the instantaneous velocity variable with its sample space V_i, ϕ_α the composition variable with sample space ψ_α. $\langle p \rangle$ is the mean pressure and p' is the pressure fluctuation. $\boldsymbol{Z}$ stands for the vector state considered in the PDF, thus $\boldsymbol{Z} = (\boldsymbol{U}, \boldsymbol{\phi})$ and $\langle A | \boldsymbol{Z} = \boldsymbol{z} \rangle$ represents the ensemble average of the generic variable A conditioned on the realization of the vector state $\boldsymbol{z} = (\boldsymbol{V}, \boldsymbol{\psi})$.

The left-hand side (LHS) of this equation is completely closed while the right-hand side (RHS) terms are not closed because of the unavailable two-point information that defines conditioned mean Laplacians [20]. Consequently, to solve Eq. (1) these terms need to be modelled. The RHS terms are respectively the *conditional acceleration* and *conditional diffusion* [29,10].

In general the solution of a modelled (closed) counterpart of Eq. (1) using standard PDE techniques (finite difference, finite volume) is computationally intractable since a great number of dimensions are involved (see e.g. [10]). For example for our case of a statistically stationary two-dimensional flow with only one scalar a five-dimensional grid would be required. The solution is more easily achieved using Monte Carlo techniques. Here we use a Lagrangian Monte Carlo method to simulate by a stochastic integration the trajectories of a sample of "fluid particles" and obtain the solution of the PDF transport equation by some sort of averaging operation [10,21]. Here, a fluid particle is intended to be a point moving with the fluid, with the local continuum fluid properties [29].

It is very important to underline the difference between true fluid particles and simulated fluid particles. Simulated fluid particles represent the real fluid only in a statistical sense; for example if we follow the trajectory of a modelled particle in the physical space we see that it is very different from that of a real fluid particle although one point statistics of the velocity field could be identical.

The stochastic system that simulates the evolution of fluid particles trajectories is

$$\mathrm{d}x_i^* = (u_i^* + \langle U_i \rangle)\, \mathrm{d}t, \tag{2}$$

$$\mathrm{d}u_i^* = a_i(\boldsymbol{x}^*, \boldsymbol{u}^*, t)\, \mathrm{d}t + b_{ij}(\boldsymbol{x}^*, \boldsymbol{u}^*, t)\, \mathrm{d}\zeta_j, \tag{3}$$

$$\mathrm{d}\phi_\alpha^* = \varphi_\alpha(\phi_\alpha^*, \boldsymbol{x}^*, \boldsymbol{u}^*, t)\, \mathrm{d}t + S_\alpha(\boldsymbol{\phi}^*)\, \mathrm{d}t, \tag{4}$$

where $\boldsymbol{x}^*$ is the modelled particle position vector, $\boldsymbol{u}^*$ the modelled particle velocity fluctuation vector, $\langle U_i \rangle$ the mean Eulerian velocity at particle location, ϕ^*_α the modelled instantaneous particle concentration of αth chemical species and S_α the scalar source/reaction term. $\mathrm{d}\zeta_j$ represents an incremental Wiener process, and asterisks identify modelled variables. a_i, b_{ij} and φ_α are, respectively, the drift, the diffusion and the micro-mixing terms.

System (2)–(4) corresponds to a Fokker–Planck (FP) equation [13] for the evolution of the model joint PDF of velocity fluctuation and composition, $f^*_{\phi u}$, that is

$$\frac{\partial f^*_{\phi u}}{\partial t} + \frac{\partial (v_i + \langle U_i \rangle) f^*_{\phi u}}{\partial x_i} = -\frac{\partial a_i f^*_{\phi u}}{\partial v_i} + \frac{\partial^2 B_{ij} f^*_{\phi u}}{\partial v_i \, \partial v_j} - \frac{\partial \varphi_\alpha f^*_{\phi u}}{\partial \psi_\alpha} - \frac{\partial S_\alpha f^*_{\phi u}}{\partial \psi_\alpha}, \tag{5}$$

where $B_{ij} = b_{ik} b_{jk}/2$.

Comparing Eq. (5) with (1) shows that the drift coefficients a_i, the diffusion coefficient b_{ij} and the micro-mixing term φ_α are modelling terms for the unclosed conditional acceleration and diffusion terms of Eq. (1). Mean velocity field is assumed to be known therefore the terms involving g_i and $\partial \langle p \rangle / \partial x_i$ in Eq. (1) are implicitly included in the drift, a_i.

To define b_{ij} we follow [23] (see also [27]) imposing the consistency with Kolmogorov similarity theory for the Lagrangian structure function in the inertial subrange,

$$b_{ij} = \delta_{ij} (C_0 \varepsilon)^{1/2}, \tag{6}$$

where C_0 is the universal constant of the Lagrangian structure function and ε is the dissipation rate of the mean turbulent kinetic energy. To define a_i we use an approach largely adopted in the study of atmospheric dispersion due to [40]; the drift coefficient is defined assuming that the one-point marginal PDF of the velocity fluctuation, $f^*_u = f^*(u_i, x_i, t)$, has a known shape (here Gaussian), built using known information about turbulent flow such as σ_{u_i}, $\langle u_i u_j \rangle$, that are obtained from measurements or theoretical assumptions (see Appendix A for further details on a_i evaluation). This definition of the coefficient guarantees the well-mixed (i.e. uniform) distribution of modelled particles into physical domain for incompressible flows (see Eq. (19)).

Once we have defined a_i and b_{ij} it remains to define a model for the micro-mixing term, φ_α. This is described in more detail in the next section.

2.2. Models for the micro-mixing term

The micro-mixing model, φ_α, describes the effect of molecular processes in the dissipation of scalar fluctuations (see e.g. [36]) and actually defines the evolution of the one-point marginal composition PDF, f_ϕ. Various micro-mixing models have been developed [7] and a set of constraints and desirable features have been proposed [10,29] to define good models. Simplifying we can restate these as: (i) at high Reynolds number the mean scalar fields must not be affected by micro-mixing; (ii) micro-mixing must dissipate the scalar fluctuations (σ_ϕ); (iii) the scalar field must be bounded (i.e., concentration must not be negative, $\phi \geqslant 0$); (iv) for homogeneous scalar fields (i.e., statistically homogeneous scalar fields in homogeneous isotropic turbulence) the scalar PDF should tend to a normal centered about the mean, $\langle \phi \rangle$. In particular, [6] argued that the PDF should tend asymptotically to a Dirac delta function about the mean, $\delta(\phi - \langle \phi \rangle)$, where the ensemble mean, $\langle \phi \rangle$ converges to a positive value in bounded domains and to zero in unbounded domain.

One of the most used micro-mixing models is the IEM introduced by [41]. The IEM assumes a linear relaxation of the scalar toward its average value:

$$\varphi_\alpha = -\frac{\phi^*_\alpha - \langle \phi^*_\alpha | x^*_i = x_i \rangle}{\tau_\mathrm{m}}, \tag{7}$$

where τ_m is the *micro-mixing timescale*. This model reflects the concept that the ultimate action of mixing is to homogenize the concentration field. Although simple, fast and widely employed in the PDF approach (for an atmospheric application see [14]), this model has been shown to have two major disadvantages. The first is the inability to respect property (iv), but this is not a necessary condition for satisfactory results in inhomogeneous flows [39]. The second is the inability to fulfill constraint (i) due to the creation of spurious fluxes, which alter the mean concentration field, as shown by [28] and further investigated by [37].

A simple alternative to IEM capable of solving the problem of spurious fluxes is the interaction by exchange with the conditional mean (IECM) model [9,28]:

$$\varphi_\alpha = -\frac{\phi^*_\alpha - \langle \phi^*_\alpha | x^*_i = x_i, u^*_i = v_i \rangle}{\tau_m}. \tag{8}$$

In this case the instantaneous scalar field relaxes to a mean that is local in physical-velocity space. Simplifying this means that particles interact with others that have a similar position and velocity. Physically this could be seen as the scalar-mixing that occurs between fluid elements that belong to the same eddy [9].

As discussed in [18] this class of mixing model is more suitable for PDF calculation involving splitting and erasing of particles then particle-interaction mixing models as, for example, modified Curl's models (see e.g. [26]).

In Section 4 we explore some differences in scalar field results obtained using IEM and IECM models since, from a discrete point of view, the IEM is just an IECM with the lowest possible resolution in the velocity space.

A problem using micro-mixing models comes with the definition of the micro-mixing timescale, τ_m. This quantity, defines the scalar fluctuations dissipation rate and depends on scalar and turbulence characteristic scales.

Under conditions of homogeneous turbulent mixing with no mean scalar gradient, $\tau_m = \tau_\phi$ and $\tau_\phi \approx \tau = e/\varepsilon$, where τ_ϕ is the dissipation time scale of concentration variance, τ the turbulence time scale, e the mean turbulent kinetic energy and ε its dissipation rate.

Several DNS simulations and laboratory experiments provide estimates of the constant of proportionality between τ_ϕ and τ (see [2] for a short summary of related experiments).

In conditions of inhomogeneous turbulent mixing (e.g., when the scalar length scale is smaller than the turbulent length scale), τ/τ_ϕ is not constant, $\tau_m \neq \tau_\phi$ and in general this time scale should be different between IEM and IECM model, though an exact formulation for τ_m is not available. However, the analysis presented here should be only weakly dependent from the value of the micro-mixing time scale.

In our simulation of releases from a localized point source (see Section 3.1) in inhomogeneous non-isotropic turbulence we use the phenomenological model for τ_m described in [2] for a neutral atmospheric boundary layer. In this model τ_m is a function of the plume relative expansion (d_r) and of the turbulent time scale (τ). See Appendix B for a brief description of the model.

3. Numerical method

We will introduce now some simple computational techniques to obtain physically consistent results maintaining affordable computational costs.

The code has been developed mainly to study the dispersion of chemical reactive species in the atmospheric environment when strong vertical mean velocity gradients and inhomogeneous turbulence conditions are present. However, in the present work the code setup is for the study of a non-reactive tracer dispersion (i.e., $\alpha = 1$) in a two-dimensional model canopy layer.

From now on, asterisks will be omitted from modelled variables, so that $x_i \equiv x^*_i$, $u_i \equiv u^*_i$ and $\phi_\alpha \equiv \phi^*_\alpha$. Moreover, we will consider $x = x_1$ and $y = x_2$ as the horizontal and vertical space coordinates, while $U = U_1$ and $V = U_2$ will be the horizontal and vertical components of instantaneous velocity field ($\langle U \rangle \neq 0$, $\langle V \rangle = 0$).

3.1. Brief description of the experimental flow and scalar field

The experiment we refer to is described extensively in [19,32,33]. In this experiment one-point statistics of velocity and passive scalar (heat) released from a line source have been measured in a wind tunnel equipped with a model canopy layer composed of metallic rods. Some experimental features are presented in Table 1. A full comparison of the model results with the measured scalar statistics up to the fourth order can be found in [5] and shows good model performance.

Velocity field statistics shown in [32,33] are sampled and used to generate profiles from polynomial interpolation, as shown in Fig. 1. These profiles are used to define both the one-point marginal Gaussian velocity

Table 1
Some simulation details

Feature	Value
Domain dimension (m)	$L_x = 1.0,\ L_y = 0.45$
Number of grid blocks	$N_b = 4$
Cell dimension ratio between adjacent grid blocks	$n = 4.0$
Scalar source position (m)	$\mu_x = 0.44,\ \mu_y = 0.051$
Scalar source sigma (m)	$\sigma_0 = 5.0 \times 10^{-3}$
Grid block number	Coordinates: $x_i = [\min, \max]$ (m)
Block 1	$x = [0.3, 1.3],\ y = [0, 0.45]$
Block 2	$x = [0.35, 0.9],\ y = [0, 0.25]$
Block 3	$x = [0.4, 0.65],\ y = [0, 0.13]$
Block 4	$x = [0.42, 0.55],\ y = [0.02, 0.095]$

PDF, $f_u = f_u^*$, from which coefficient a_i is obtained and both the dissipation ε from which the coefficient b_{ij} is computed (see Appendix A). The validity of the Gaussian approximation for dispersion inside a canopy has been explored by several investigators (see e.g. [8,25]).

3.2. Monte Carlo code and block-structured grid

As discussed above, the best way to solve the joint velocity-composition PDF equation uses a Monte Carlo integration of the differential equations shown in Eqs. (2)–(4). What we obtain is a set of N_p trajectories in the phase space, (x_i, u_i, ϕ_α), which are a statistical representation of the fluid movement and scalar dispersion processes. This means that by adopting kernel averaging we estimate all the moments of the process modelled by the stochastic system at a given position in space, x_i. Here we use a particle-mesh method with cell centered statistics. Therefore, the domain is covered with a mesh and the kernel estimates are related to each cell center (see e.g. [10,29]).

3.2.1. Block-structured grid

Considering a typical computational domain for a short range prediction of atmospheric pollution the ratio between the characteristic length scale of the source and the size of the domain can be easily less then 10^{-3}. The grid should be refined in order to provide details of the concentration field around the scalar source and as a consequence, a large number of particles need to be simulated in order to have meaningful statistics at each grid point. Because in PDF calculations the computational cost (W) is directly related to the number of particles per cell ($N_p^{(i_c)}$ where $i_c = 1, \ldots, N_c$ is the cell index), the number of cells (N_c) and the total number of time steps (N_t), i.e.,

$$W \simeq N_t \sum_{i_c=1}^{N_c} N_p^{(i_c)} = N_t N_p, \tag{9}$$

it could be necessary to use some kind of locally-refined grid. As outlined in Section 1 unstructured grids can be used but their use is computationally expensive and they are not required to have satisfactory performance in scalar PDF calculation. In this work, computational costs have been lightened by adopting a block-structured grid approach.

The grid is composed of N_b blocks (subgrids) of different dimensions and resolutions. The smaller blocks are nested within the bigger ones. The grid system is shown in Fig. 2. The characteristic dimension of cells in the lth grid block is an integer fraction of that in the $(l-1)$th grid block

$$\Delta x^{(l)} \Delta y^{(l)} = \frac{\Delta x^{(l-1)} \Delta y^{(l-1)}}{n}, \tag{10}$$

where $n(=4)$ is the ratio between the cell size of neighbor blocks (see Table 1). The quantitative characteristic of the grid structure can be deduced from Tables 1 and 2. All the grid resolutions used in the simulations are

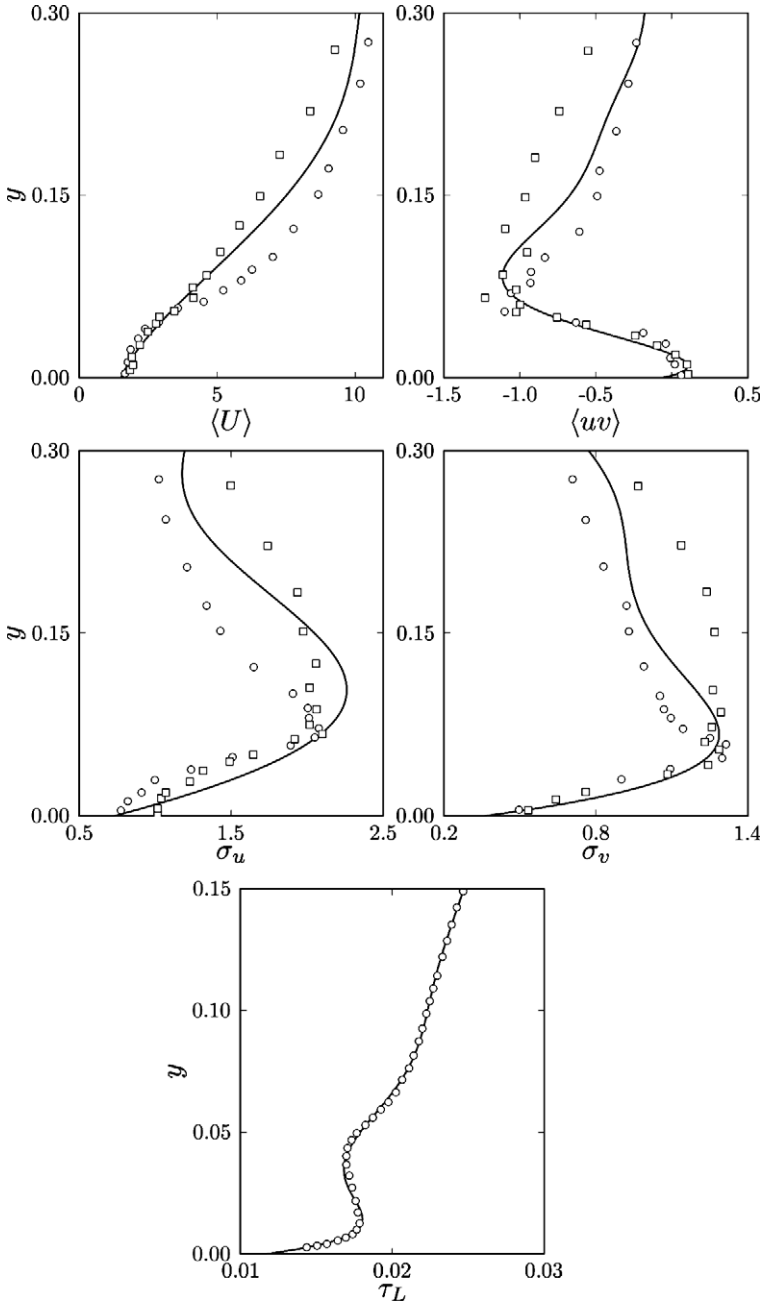

Fig. 1. Velocity statistics input profiles obtained from [32,33] experiment, used to define coefficients a_i and b_{ij}.

reported in Table 2. Some calculation performances are given in Table 3 for different grid setups and model configurations.

We point out that the block-structured grid allows for more complex grid configuration than that shown here and is enough flexible to treat multiple source configurations and complex geometry (urban environment), thus being an optimal tool for atmospheric dispersion predictions.

Because of the globally non-uniform cell dimensions, a splitting/erasing (SE) algorithm has been introduced for error-reduction purposes (see Fig. 3) as will be fully discussed below.

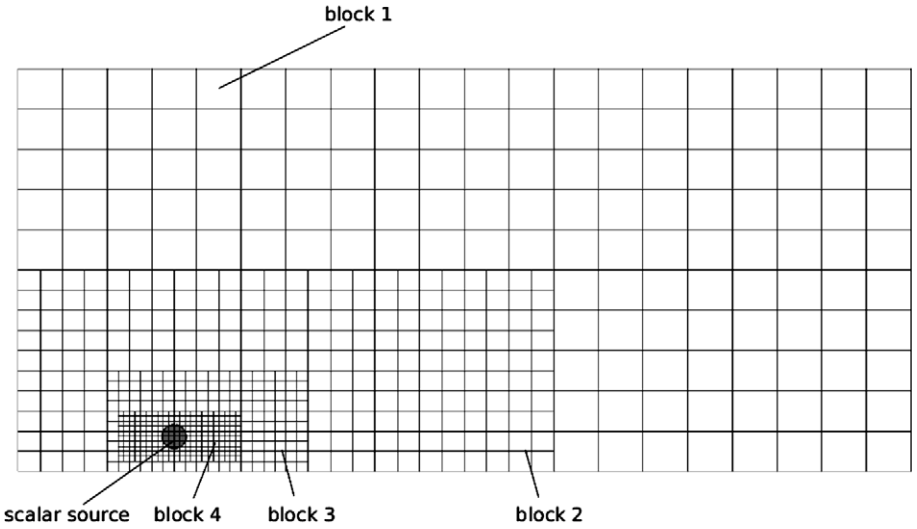

Fig. 2. Representation of the block-structured grid of dimension $L_x \times L_y = 1 \times 0.45$, discretized with $N_c = 680$ cells. The scalar source location $(0.44, 0.051)$ is centered on block 4.

Table 2
Grid settings employed to evaluate discretization error

Setting	Properties: $\Delta x_i = [\min, \max]$ (m), N_c
1 (○)	$\Delta x = [6.3 \times 10^{-3}, 5.0 \times 10^{-2}]$, $\Delta y = [5.6 \times 10^{-3}, 4.5 \times 10^{-2}]$, 773
2 (□)	$\Delta x = [5.0 \times 10^{-3}, 4.0 \times 10^{-2}]$, $\Delta y = [4.7 \times 10^{-3}, 3.75 \times 10^{-2}]$, 1152
3 (△)	$\Delta x = [4.2 \times 10^{-3}, 3.33 \times 10^{-2}]$, $\Delta y = [3.7 \times 10^{-3}, 3.0 \times 10^{-2}]$, 1743
4 (◇)	$\Delta x = [3.1 \times 10^{-3}, 2.5 \times 10^{-2}]$, $\Delta y = [2.2 \times 10^{-3}, 1.8 \times 10^{-2}]$, 3928

Symbols refer to curves in Figs. 13 and 14.

3.2.2. Computational algorithm

The computational algorithm is composed of the following main steps:

- **Initialization of particle properties**, (x_i, u_i, m, ϕ);
- **Main time loop**, $(T = T + \Delta t^{(g)})$;
  - **Time loop on every particle**, $(T^{(loc)} = T^{(loc)} + \Delta t^{(loc)})$:
    Update (x_i, u_i) from Eqs. (2) and (3);
    Apply boundary conditions (see below);
    Apply Splitting/Erasing (update m and N_p);
    Update ϕ using Eq. (4);
    Account for scalar source $(\phi = \phi_s(x, y))$;
  - **Update cell-centered statistics**, ($\widetilde{\phi}_{i_c}$, $\widetilde{\phi^2}_{i_c}$, etc) using Eq. (16);
- **Calculate time averaged statistics**, ($\overline{\phi}_{i_c}$, σ_ϕ, etc.) using Eq. (30).

A set of N_p stochastic particles of computational weight m are initially distributed with uniform density (see Eq. (19)) in a physical domain of dimension $L_x \times L_y = 1. \times 0.45\ \mathrm{m}^2$, discretized with a block-structured grid, and then moved in phase-space (x_i, u_i, ϕ) by numerically integrating the stochastic system (2)–(4) using an Euler–Maruyama integration scheme, which has a first order convergence in weak sense (see e.g. [16]). At the end of every local time step, $\Delta t^{(loc)}$, near-source particles are marked by a scalar concentration, $\phi_s(x, y)$ defined around the source by a two-dimensional Gaussian function,

Table 3
Some computation performances by varying some simulation parameters

Mixing model	Grid setting (Table 2)	Nested	SE	$N_p^{(i_c)}$	$t_s^{(adim)}$
Increasing particle number, nested grid					
IEM	Setting 1	Yes	Yes	14	1
IEM	Setting 1	Yes	Yes	44	3
IEM	Setting 1	Yes	Yes	88	6
IEM	Setting 1	Yes	Yes	147	10
Changing mixing model, nested grid (Section 4.2)					
IEM	Setting 2	Yes	Yes	620	107
IECM (3×3)	Setting 2	Yes	Yes	620	120
IECM (9×9)	Setting 2	Yes	Yes	620	125
IECM (27×27)	Setting 2	Yes	Yes	620	135
Increasing cell resolution (IEM), nested grid					
IEM	Setting 1	Yes	Yes	88	6
IEM	Setting 2	Yes	Yes	88	14
IEM	Setting 3	Yes	Yes	88	32
IEM	Setting 4	Yes	Yes	88	45
Increasing cell resolution (IECM 9×9), nested grid					
IECM (9×9)	Setting 1	Yes	Yes	88	6.5
IECM (9×9)	Setting 2	Yes	Yes	88	15
IECM (9×9)	Setting 3	Yes	Yes	88	34
IECM (9×9)	Setting 4	Yes	Yes	88	50
Increasing cell resolution, regular grid					
	$\Delta x\times\Delta y$, N_c				
IEM	$6.3\times10^{-3}\times5.6\times10^{-3}$, 12,720	No	No	88	61
IEM	$4.2\times10^{-3}\times3.7\times10^{-3}$, 28,798	No	No	88	148
IEM	$3.1\times10^{-3}\times2.2\times10^{-3}$, 65,688	No	No	88	332

Time required for each global time step ($t_s^{(adim)}$) is in adimensional form. Grid settings for nested grid refer to Table 2.

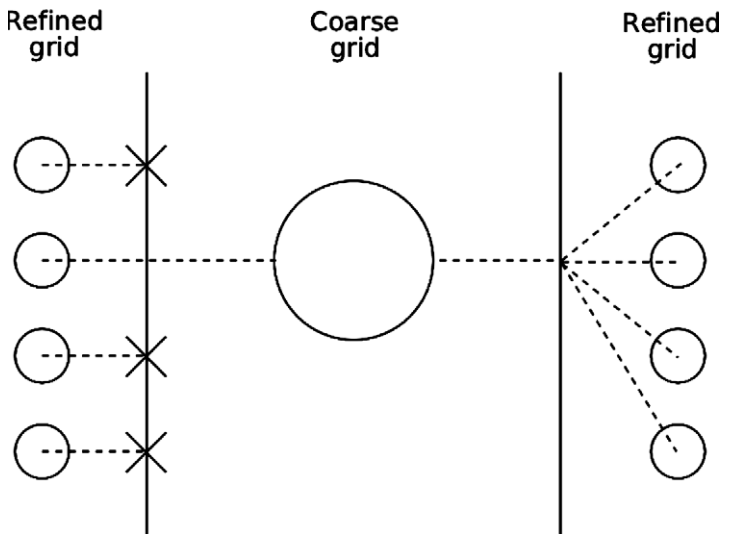

Fig. 3. Sketch of the particle erasing procedure (left) with probability 3/4 when entering a coarser grid block. The surviving particle retains its characteristics while the computational weight (m) is increased. Particle splitting (right) when entering a refined grid block, the new particles have a computational weight 1/4 of the mother particle.

$$\phi_s(x,y)=\frac{\mathscr{Q}(\Delta t^{(loc)})}{2\pi\sigma_0^2}\exp\left[\frac{(x-\mu_x)}{2\sigma_0^2}+\frac{(y-\mu_y)}{2\sigma_0^2}\right], \tag{11}$$

where $\mathscr{Q}(\Delta t^{(\mathrm{loc})})$ is the source strength, $\sigma_0 = 5.0 \times 10^{-3}$ m the source diameter and $(\mu_x = 0.44, \mu_y = 0.051)$ m the source position.

When particles arrive in boundary regions, the following conditions are imposed:

- top boundary, perfect reflection of particles velocity and position and absorption of the concentration;
- bottom boundary, perfect reflection of particles velocity and position while the concentration is not changed;
- left and right boundaries, periodic condition for particles velocity and position and absorption of the concentration.

At the end of every global time step cell-centered statistics, $\widetilde{\phi}^n_{i_c}$ are updated; the new calculated values of $\widetilde{\phi}_{i_c}$ are used during the next global time step in the micro-mixing process.

With the SE algorithm all the cells in the domain have (statistically) the same number of particles $N_{\mathrm{p}}^{(i_c)}$, during the whole simulation. See Fig. 4 for a plot of the instantaneous and mean, $N_{\mathrm{p}}^{(i_c)}$. Each particle has a weight, m, which depends on the size of the cell within which it is located: smaller the cell smaller will be m. More precisely m is a function of the grid "level", l, in which particle is located,

$$m = 1/n^{l-1}. \tag{12}$$

The SE algorithm is composed of two parts:

particle splitting: when a particle of weight m starting from a cell of grid $l-1$ arrives in a cell of grid l it is split into n "children" particles. These particles inherit all the features of the mother particle (u, v, x, y, ϕ) except the computational weight that becomes m/n. On successive time steps these n particles become independent. In other terms we can consider splitting as a "ramification" of a trajectory of the stochastic process into n independent trajectories starting from the same initial state.

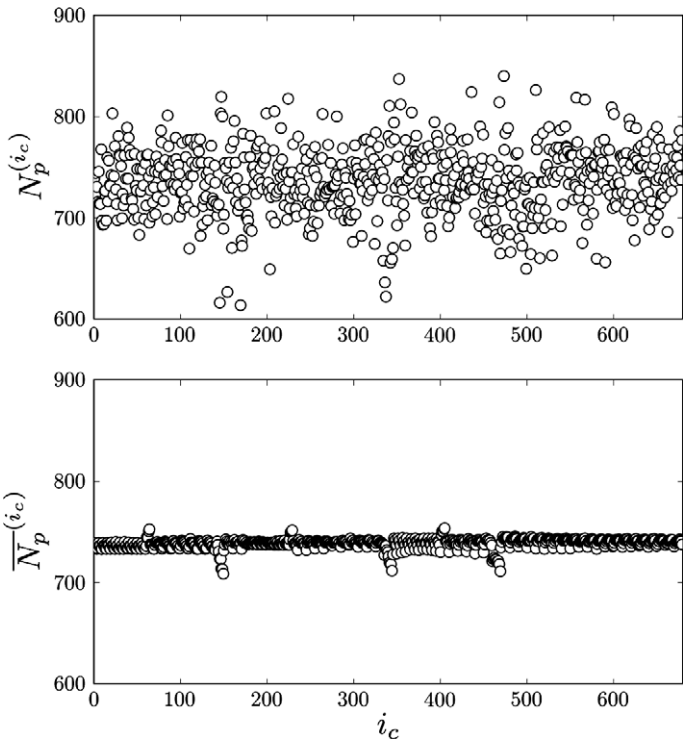

Fig. 4. Instantaneous $(N_{\mathrm{p}}^{(i_c)})$ and time-averaged $(\overline{N_{\mathrm{p}}^{(i_c)}})$ particle number, in each grid cell $(i_c = \{1, \ldots, N_c\})$.

particles erasing: when a particle of weight m starting from a cell of grid l arrives in a cell of grid $l-1$ it has a probability $q_1 = 1/n$ to proceed and a probability $q_2 = (n-1)/n$ to be erased. The weight of the "surviving" particles becomes n times the original one: $n \times m$.

The SE procedure used here is simpler compared to others used in the literature (see e.g. [18,38]) since it is directly related to the ratio of adjacent cells size. More specifically, it does not need any control of the total mass (computational weight) in each cell, any sorting algorithm to decide the particle to be split and any artificial threshold to decide what particle should be split and when. The method is straightforward to apply in structured grid and it could be also applied to unstructured grid although with a lower efficiency.

Every (global) time step is composed of a series of time sub-steps; every particle is moved respecting a local *extended Courant criteria*,

$$\max\left(\frac{\Delta t^{(\mathrm{loc})}(u+\langle U\rangle)}{\Delta x_{i_c}}, \frac{\Delta t^{(\mathrm{loc})}\sigma_v}{\Delta y_{i_c}}, \frac{\Delta t^{(\mathrm{loc})}\varepsilon}{e}, \frac{\Delta t^{(\mathrm{loc})}}{\tau_{\mathrm{m}}}\right) < 1, \tag{13}$$

where $\Delta t^{(\mathrm{loc})}$ is the position-dependent (local) time step of each particle; here σ_{v} is the standard deviation of the vertical velocity. The *local time step* is thus defined as,

$$\Delta t^{(\mathrm{loc})} = \min\left(\alpha^{(\mathrm{loc})}\frac{\Delta x_{i_c}}{(u+\langle U\rangle)}, \alpha^{(\mathrm{loc})}\frac{\Delta y_{i_c}}{\sigma_v}, \alpha^{(\mathrm{loc})}\frac{e}{\varepsilon}, \alpha^{(\mathrm{loc})}\tau_{\mathrm{m}}\right), \tag{14}$$

where $0 < \alpha^{(\mathrm{loc})} < 1$. All the variables involved in this equation are evaluated at particle location (x, y). Using position-dependent time steps allows one to avoid unnecessary calculations for particles located in greater cells since these can be moved using a longer $\Delta t^{(\mathrm{loc})}$.

Particles are synchronized using a *global time step*, $\Delta t^{(\mathrm{g})}$,

$$\Delta t^{(\mathrm{g})} = \alpha^{(\mathrm{g})}\frac{\Delta x^{(l=1)}}{\max(\langle u\rangle)}, \quad 0 < \alpha^{(\mathrm{g})} < 1. \tag{15}$$

A condition is imposed on $\Delta t^{(\mathrm{loc})}$ to ensure that $T^{(\mathrm{loc})} + \Delta t^{(\mathrm{loc})} \leqslant \Delta t^{(\mathrm{g})}$. We note that under stationary conditions an alternative more rigorous method of local time stepping can be used [22]. This method is perfectly consistent and very simple to implement when coupled to a posteriori treatment of particles distribution.

When $T^{(\mathrm{loc})} + \Delta t^{(\mathrm{loc})} = \Delta t^{(\mathrm{g})}$ cell-centered statistics are updated using the following averaging operation (Q is a generic variable, such as $\phi, \ldots, \phi^n$),

$$\widetilde{Q}_{i_c} = \frac{\sum_{j=1}^{N_{\mathrm{p}}} \widehat{\mathscr{K}}(\boldsymbol{x}_j) Q_j m_j T_j^{(r)}}{\sum_{j=1}^{N_{\mathrm{p}}} \widehat{\mathscr{K}}(\boldsymbol{x}_j) m_j T_j^{(r)}}, \tag{16}$$

where $T_j^{(r)}$ is the residence time of particle j in each cell during a global time step, $\widehat{\mathscr{K}}$ is the kernel function defined as

$$\widehat{\mathscr{K}}(\boldsymbol{x}_j) = \begin{cases} 1 & \text{if } \boldsymbol{x}_{i_c} < \boldsymbol{x}_j < \boldsymbol{x}_{i_c} + \Delta\boldsymbol{x}_{i_c}, \\ 0 & \text{otherwise.} \end{cases} \tag{17}$$

This vector inequality means that the particle j is selected for the average in the physical cell i_{c} if it is contained inside the cell. This kind of kernel has the desirable properties to respect both local and global mean conservation [10]. In our case we cannot find any significant improvement in the results using a more spatially accurate kernel. The mean number of particles present in the cell i_{c} during a $\Delta t^{(\mathrm{g})}$ is given by

$$N_{\mathrm{p}}^{(i_c)} = \frac{\sum_{j=1}^{N_{\mathrm{p}}} \widehat{\mathscr{K}}(\boldsymbol{x}_j) m_j T_j^{(r)}}{m^{(i_c)} \Delta t^{(\mathrm{g})}}, \tag{18}$$

where $m^{(i_c)}$ represents the characteristic weight of particles in cell i_{c}. Particle density within a cell is given by

$$\rho_{\mathrm{p}}^{(i_c)} = \frac{\sum_{j=1}^{N_{\mathrm{p}}} \widehat{\mathscr{K}}(\boldsymbol{x}_j) m_j T_j^{(r)}}{\Delta x \Delta y \Delta t^{(\mathrm{g})}}; \tag{19}$$

in incompressible flows $\rho_{\mathrm{p}}^{(i_c)}$ is statistically homogeneous in space and time.

In this setup, particle cell localization is a trivial and fast task. Cells are numbered sequentially using the simple formula,

$$i_c = (k_x - 1)N_y^{(l)} + k_y + N_c^{(1:l-1)}, \tag{20}$$

where $N_y^{(l)}$ represents the number of cells in y direction at grid block l, $N_c^{(1:l-1)}$ is the total number of cells included in subgrid 1 to $l-1$, k_x and k_y are the local indexes of the cell in its block, respectively, in the x and y directions.

When velocity conditioned averages are required (i.e., in IECM micro-mixing), computational cells extend also in velocity space and cell-centered statistics are calculated using

$$\widetilde{Q}_{i_{vc}} = \frac{\sum_{j=1}^{N_p} \widehat{\mathscr{K}}(\boldsymbol{x}_j, \boldsymbol{u}_j) Q_j m_j T_j^{(r)}}{\sum_{j=1}^{N_p} \widehat{\mathscr{K}}(\boldsymbol{x}_j, \boldsymbol{u}_j) m_j T_j^{(r)}}, \tag{21}$$

where $T_j^{(r)}$ now refers to cells in (x_i, u_i)-space, i_{vc} is the index of space-velocity cells, and the kernel estimator is,

$$\begin{aligned} &\widehat{\mathscr{K}}(\boldsymbol{x}_j, \boldsymbol{u}_j) = 1 \quad \text{if } \boldsymbol{x}_{i_{vc}} < \boldsymbol{x}_j < \boldsymbol{x}_{i_{vc}} + \Delta\boldsymbol{x}_{i_{vc}} \text{ and } \boldsymbol{u}_{i_{vc}} < \boldsymbol{u}_j < \boldsymbol{u}_{i_{vc}} + \Delta\boldsymbol{u}_{i_{vc}}, \\ &\widehat{\mathscr{K}}(\boldsymbol{x}_j, \boldsymbol{u}_j) = 0 \quad \text{otherwise.} \end{aligned} \tag{22}$$

This vector inequality means that the particle j contributes to the average in (21) if it is contained inside the cell of index i_{vc} in the four-dimensional physical-velocity space. Velocity space discretization is achieved by creating cells of equal-probability in the u_i domain. For example, if we assume a Gaussian shape for the PDF of the horizontal velocity fluctuation (see Section 2.1), u, given by

$$G(u) = \frac{1}{\sigma_u \sqrt{2\pi}} \exp[-u^2/2\sigma_u^2], \tag{23}$$

to discretize the u-space we require that

$$\int_{u_k}^{u_{k+1}} G(w)\, \mathrm{d}w \approx \int_{-\infty}^{+\infty} G(w)\, \mathrm{d}w / N_{vc} \quad \text{for each } k, \tag{24}$$

where $k = \{1, \ldots, N_{vc}\}$ and N_{vc} represent the node index and the number of cells of the velocity grid.

When velocity components are correlated (i.e., $\langle uv \rangle \neq 0$) the reference system is modified to simplify the cell creation (see Appendix C for more details).

4. Numerical testing

Solving a physical problem by numerical methods is always a delicate task, and the main efforts in developing a numerical code are finalized on obtaining an accurate solution while minimizing the computational costs.

4.1. Computational errors

Following [43], numerical error ($\mathscr{E}_Q$, where Q represents a generic computed quantity, i.e. a scalar statistic) can be defined as the sum of two components: *statistical error* (S_Q), and *deterministic error* ($\mathscr{D}_Q$), so that it reduces to

$$\mathscr{E}_Q = S_Q + \mathscr{D}_Q. \tag{25}$$

The two errors have different origins and behaviors.

4.1.1. Statistical error

The statistical error (S_Q) is due to the fact that the number of particles representing the joint PDF in each cell, $N_p^{(i_c)}$ is finite. If we consider a generic variable Q, for which we calculate an instantaneous cell-centered statistic, using Eq. (16), S_Q is defined as,

$$S_Q = \widetilde{Q}_{i_c} - \langle \widetilde{Q}_{i_c} \rangle. \tag{26}$$

The second term in RHS represents the ensemble average of the instantaneous cell-centered mean.

In the left plot of Fig. 5 we show the evolution of the instantaneous cell-centered mean concentration, $\widetilde{\phi}_{i_c}$, for different measurement points. For simulation times within the stationary regime (i.e., $T > T_s \approx 0.5$ s), the fluctuations around $\langle \widetilde{\phi}_{i_c} \rangle$ are caused by the statistical error.

Fig. 6 shows the root-mean-squared (rms) statistical error of $\widetilde{\phi}_{i_c}$ and $\widetilde{\sigma_\phi} = (\widetilde{\phi^2} - \widetilde{\phi}^2)^{1/2}$ as a function of the cell particle number $N_p^{(i_c)}$ for IEM and IECM 9×9 mixing models, both with and without SE algorithm. From now on $N_u \times N_v$ will be used to point out the number of velocity classes used by the IECM model (i.e., 9×9 means that the velocity space is discretized with $N_{u_i} = 9$ cells in both u and v directions for a total of 81 cells). The expected relation,

$$S_Q = \frac{\alpha_Q}{\sqrt{N_p^{(i_c)}}} \vartheta, \tag{27}$$

is confirmed: the statistical error is a function of the square root of the cell particle number. Here α_Q is the slope of the fit lines and ϑ is a standardized random variable (we can see also that $S_Q = \sigma_Q / \sqrt{N_p^{(i_c)}} \vartheta$, [43]). The number of $N_p^{(i_c)}$ for the NSE (no splitting/erasing) simulation is different at different measurement points since they are located in different grid blocks.

For different measurement points, given the same $N_p^{(i_c)}$, the statistical error can vary significantly.

An alternative and more relevant representation of the instantaneous error, within a stationary regime, is shown in right plot of Fig. 5. This is the relative error and is given by the concentration fluctuation, $(\widetilde{\phi}_{i_c} - \overline{\phi}_{i_c})$ normalized by the time-averaged concentration (see Eq. (29)), $\overline{\phi}_{i_c}$,

$$[\overline{\phi}_{i_c}]_R = \frac{(\widetilde{\phi}_{i_c} - \overline{\phi}_{i_c})}{\overline{\phi}_{i_c}}. \tag{28}$$

Differences between temporal series are due to different turbulence and scalar mixing characteristics in the flow. The statistical error of $[\overline{\phi}_{i_c}]_R$ and $[\sigma_\phi]_R$ approximately collapse on the same curve in Fig. 7, for different measurement points. This is more evident when the SE algorithm is used since the statistical error tends to be only a function of the $N_p^{(i_c)}$ and irrespective of the location. However, the collapse is not perfect showing that there is still a weak dependence on the location.

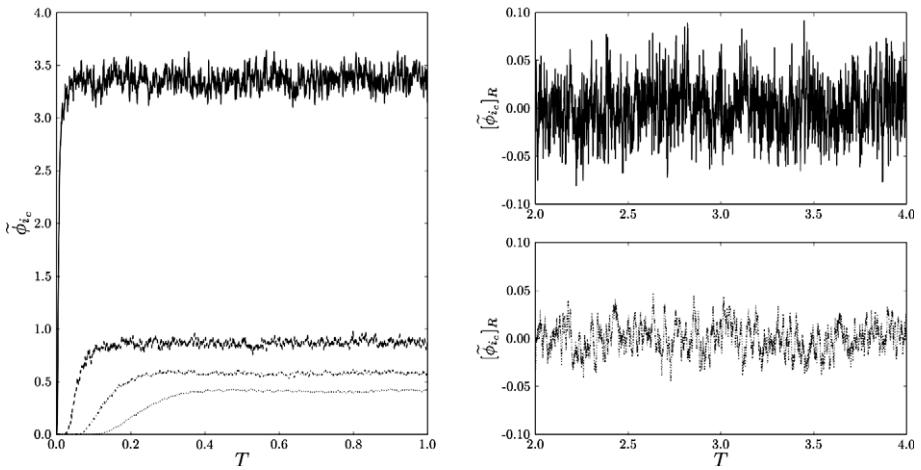

Fig. 5. Left: time evolution of the instantaneous i_cth cell-centered mean concentration, $\widetilde{\phi}_{i_c}$. Different curves represent different measurement points: continuous line (0.46, 0.047), dashed line (0.6, 0.047), dash-dotted line (0.8, 0.047) and dotted line (1.136, 0.047). T is the simulation time (s). Right: time evolution of the instantaneous relative error of $\widetilde{\phi}_{i_c}$ on $\overline{\phi}_{i_c}$, in two different locations: continuous line (0.46, 0.047), dotted line (1.136, 0.047). T is the simulation time (s). $N_p^{(i_c)} = 88$ and grid corresponds to setting 1.

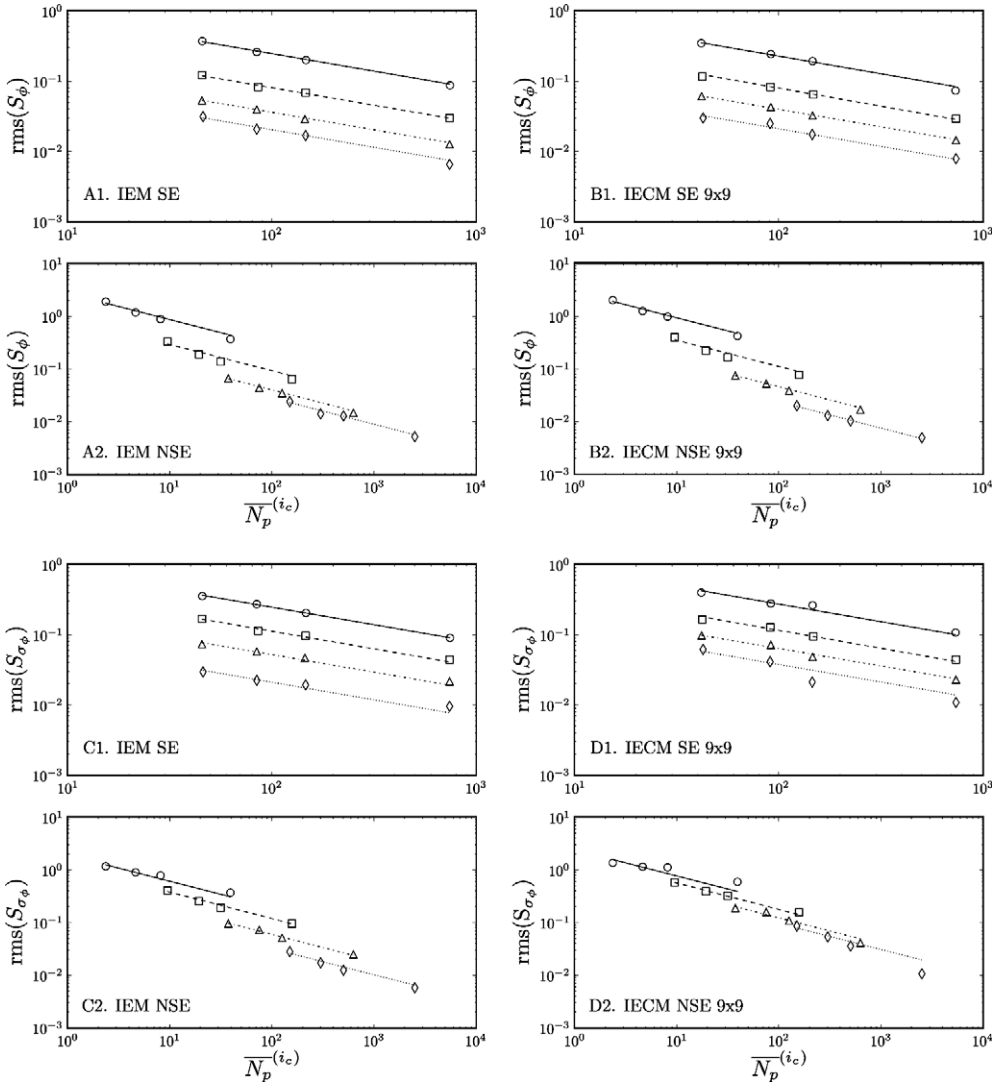

Fig. 6. Root-mean-squared (rms) statistical error of the instantaneous cell-centered mean concentration ($\widetilde{\phi}_{i_c}$, A1 to B2) and scalar variance ($\widetilde{\sigma}_\phi$, C1 to D2). Top plots (A1, B1, C1 and D1) refer to simulation with SE algorithm while bottom plots (A2, B2, C2 and D2) refer to simulations without SE algorithm (NSE). Left column plots refer to IEM micro-mixing model, while right column plots refer to IECM (9×9). Measurement points are (0.46, 0.047: ○), (0.6, 0.047: □), (0.8, 0.047: △) and (1.136, 0.047: ◇). Grid corresponds to setting 1.

In Fig. 6 we can evaluate the statistical error reduction induced by the splitting/erasing algorithm, especially in regions with smaller cells (symbols ○ and □) where, without SE, $N_{\mathrm{p}}^{(i_c)}$ is very small if compared with larger cell regions. Therefore, maintaining constant the total number of particles, N_{p}, the SE algorithm results in a significant reduction of the statistical error in the near source region. Moreover, using the SE procedure the statistical error is more uniform in the entire domain.

For statistically stationary time series, statistical error can be further reduced via time-averaging,

$$\overline{Q}_{i_c} = \overline{\widetilde{Q}}_{i_c} = \frac{1}{T_{\mathrm{av}}} \int_{T_s}^{T_s+T_{\mathrm{av}}} \widetilde{Q}_{i_c}(s)\, \mathrm{d}s, \tag{29}$$

calculated using

$$\overline{Q}_{i_c} = \frac{\sum_{k=1}^{N_t} \widetilde{Q}_{i_c}^{(k)}}{N_t}, \tag{30}$$

where (k) refers to the kth global time step.

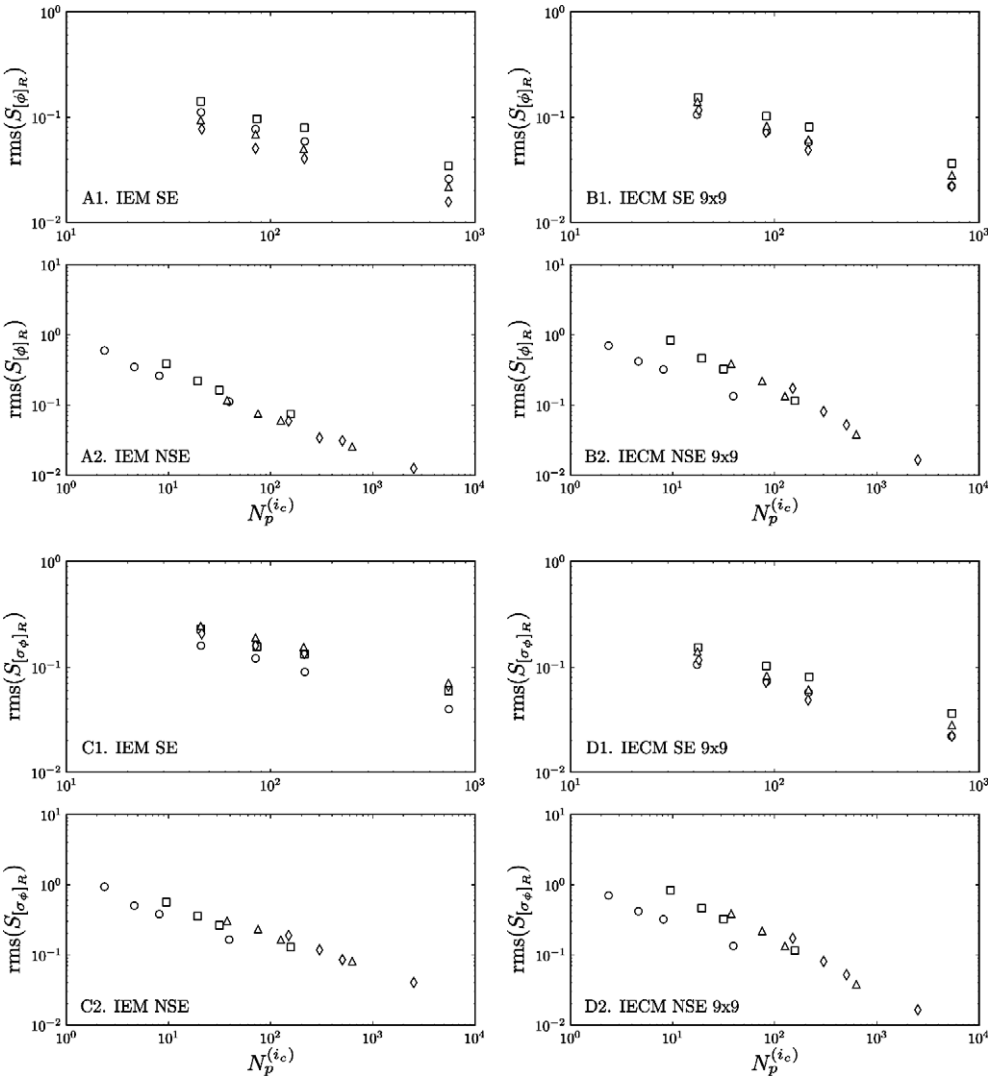

Fig. 7. As in Fig. 6 but for the statistical error of the relative errors $[\widetilde{\phi}]_R$ and $[\sigma_\phi]$. Measurement points are (0.46, 0.047: ○), (0.6, 0.047: □), (0.8, 0.047: △) and (1.136, 0.047: ♢). Grid corresponds to setting 1.

In Fig. 8 we show a comparison between the instantaneous cell-centered mean concentration $\widetilde{\phi}_{i_c}$ and the time-averaged concentration $\overline{\phi}_{i_c}$ for increasing averaging time T_{av} (once the process has reached its stationary state). It is easy to see that the variance of the time-averaged variables decreases with increasing T_{av}, thus removing the presence of statistical errors.

A measure of this variance reduction obtained from a series of 30 independent IEM simulations is shown in Fig. 9 where the variance reduction factor of the time averaged concentration is plotted against the averaging time. For generic quantity Q the variance reduction factor is defined [30,43] as

$$\mathscr{R}_Q = \left[\frac{\mathrm{var}(\overline{Q}_{i_c})}{\mathrm{var}(\widetilde{Q}_{i_c})}\right]^{1/2}, \tag{31}$$

where "var" stands for the variance computed using the 30 independent simulations just mentioned. Fig. 9 shows that to reduce the statistical error by time averaging we need to average for a time T_{av} that is longer than a factor of the time scale $t_Q^{(c)}$. $t_Q^{(c)}$ represents the correlation time of the time series and consequently,

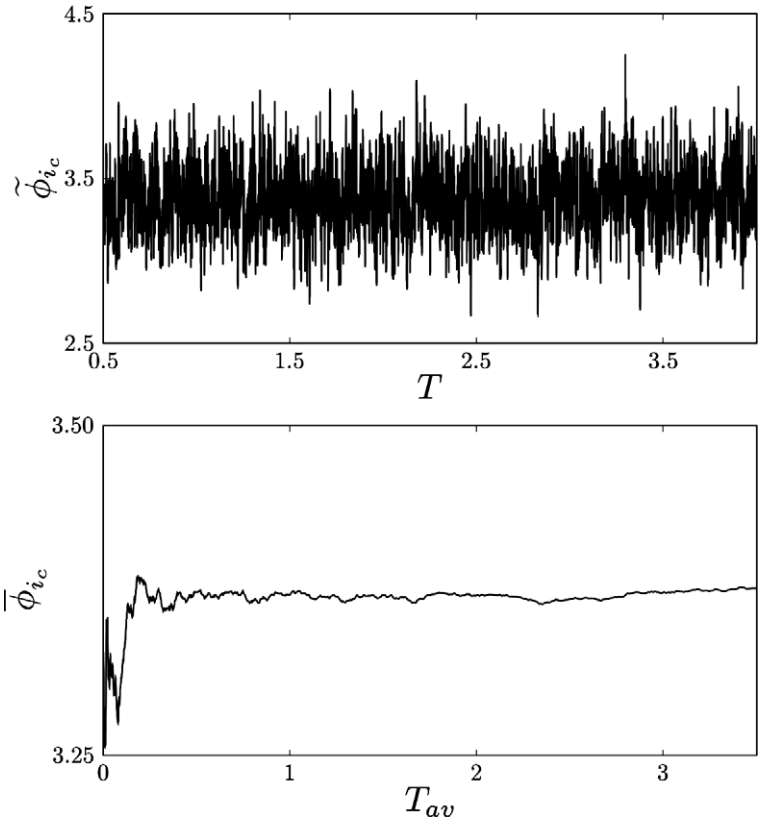

Fig. 8. Instantaneous cell-centered mean concentration $\widetilde{\phi}_{i_c}$ (top) and time averaged mean concentration $\overline{\phi}_{i_c}$ (bottom) as a function of the simulated time T (s) and the averaging-time T_{av} (s). $N_{\mathrm{p}}^{(i_c)} = 88$ and the grid corresponds to setting 1.

the efficiency in reducing the statistical error using time-averaging technique. In particular, $t_{\phi}^{(\mathrm{c})}$ shown in Fig. 9 can be found by fitting the curve of $\mathscr{R}_Q$ (for $Q \equiv \phi$) in the region of steeper slope. Alternatively $t_{\phi}^{(\mathrm{c})}$ can always be computed as the integral of the autocorrelation function, $r_{\phi}(s) \equiv \langle \widetilde{\phi}(t)\widetilde{\phi}(t+s)\rangle$ of the series,

$$t_{\phi}^{(\mathrm{c})} = \int_0^{\infty} r_{\phi}(s)\,\mathrm{d}s. \tag{32}$$

As we see in Fig. 9, the value of $t_{\phi}^{(\mathrm{c})}$ and $t_{\sigma_{\phi}}^{(\mathrm{c})}$ (slope of linear fits) is not homogeneous in the whole domain: it depends on local characteristics of turbulence and micro-mixing process. In general where signal fluctuations have lower frequencies (greater $t_Q^{(\mathrm{c})}$), the averaging time requested to reduce significantly the statistical error will be longer.

Averaging time in the order of 100 times $t_Q^{(\mathrm{c})}$ can reduce the statistical error by two orders of magnitude. Although Fig. 9 refers to IEM simulation with SE, the same consideration extends to IECM results.

4.1.2. Deterministic errors

Statistical error plays a fundamental role in error analysis but another major contribution to the inaccuracy of the numerical solution comes from deterministic errors, $\mathscr{D}_Q$. $\mathscr{D}_Q$ originates from the use of discrete mathematics in solving differential equations. In particular, we can separate deterministic errors in two main parts: *bias* (B_Q) and *discretization* error (D_Q).

Bias, B_Q, results from using a finite number of particles. We can define the bias as the difference between the time-averaged solution with $N_{\mathrm{p}}^{(i_c)}$ particles, and the solution obtained for $N_{\mathrm{p}}^{(i_c)} \to \infty$, maintaining constants all other simulation features ($N_{\mathrm{c}}, \Delta t$),

$$B_Q(N_{\mathrm{p}}^{(i_c)}) = \overline{Q(N_{\mathrm{p}}^{(i_c)})}_{i_c} - \overline{Q(\infty)}_{i_c}. \tag{33}$$

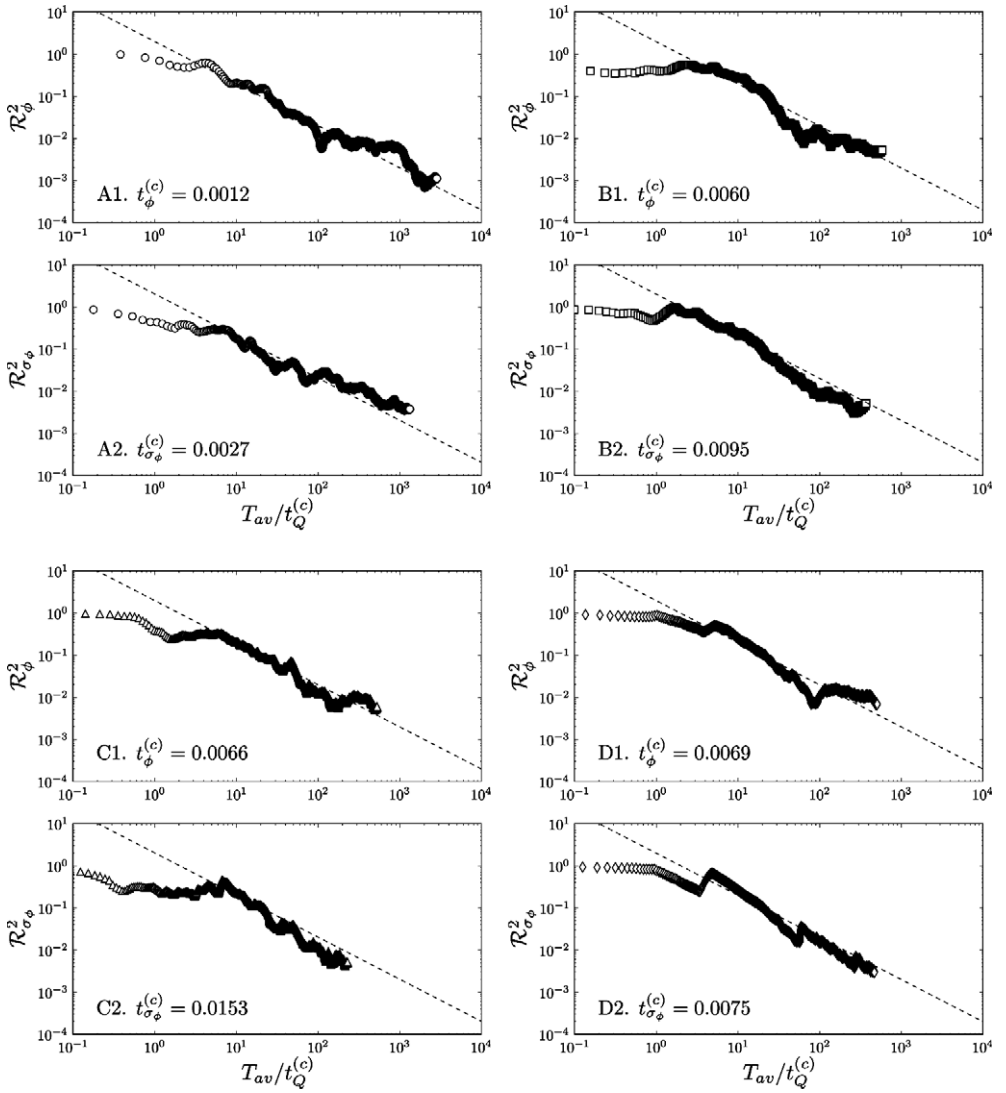

Fig. 9. Reduction factor of the scalar statistical error of $\widetilde{\phi}_{i_c}$ (upper plots, A1, B1, C1, D1) and σ_ϕ (lower plots, A2, B2, C2, D2), plotted as a function of the averaging-time T_{av} normalized on the correlation time $t_Q^{(c)}$, for IEM simulations. Different symbols refer to different locations in the computational domain (0.46, 0.047: ○), (0.6, 0.047: □), (0.8, 0.047: △) and (1.136, 0.047: ◇). $N_{\mathrm{p}}^{(i_c)} = 88$ and the grid corresponds to setting 1. The dashed line represents $2/T_{\mathrm{av}}$ slope.

In general, since we do not know the value of $\overline{Q(\infty)}_{i_c}$, we need to adopt another procedure to evaluate the bias. In Fig. 10 we show the value of $\overline{\phi}_{i_c}$ for different values of $N_{\mathrm{p}}^{(i_c)}$. Increasing $N_{\mathrm{p}}^{(i_c)}$ results in a decrease of B_Q following the relation

$$B_Q = \frac{b_Q}{N_{\mathrm{p}}^{(i_c)}}, \tag{34}$$

where the bias coefficient b_Q is an empirical constant which can be deduced from the slopes of the linear fits in Fig. 10. Bias plots obtained from Eq. (34) are shown in Fig. 10.

Values of b_ϕ are shown in Fig. 10. The first aspect we notice from these plots is that IECM solutions are more sensitive to the cell particle number $N_{\mathrm{p}}^{(i_c)}$ than IEM solutions. This is an expected behavior because in the IECM model particles need to be located also in velocity space; the computational grid is four-dimensional (x, y, u, v). For this reason, a velocity-conditioned mixing model requires a greater number of total particles

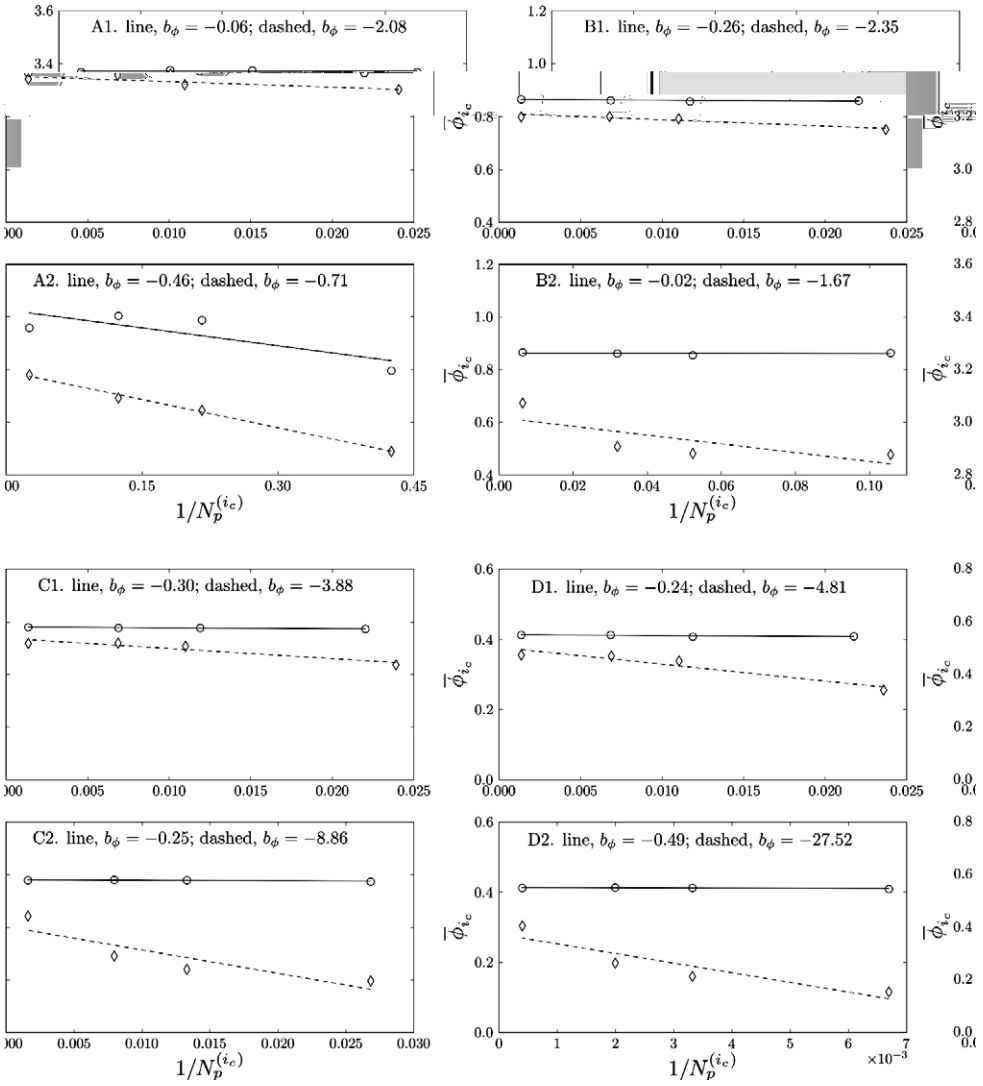

Fig. 10. Time-averaged concentration $\overline{\phi}_{i_c}$ as a function of the cell particle number, $N_{\mathrm{p}}^{(i_c)}$. IEM (○) and IECM 9×9 (◇) results are shown both with SE algorithm (A1, B1, C1 and D1) and without SE algorithm (NSE, A2, B2, C2 and D2). Bias coefficient, b_ϕ, is included at the top of plots. Measurement points are (0.46, 0.047: A), (0.6, 0.047: B), (0.8, 0.047: C) and (1.136, 0.047: D). Grid corresponds to setting 1.

(N_{p}) to reach the same level of bias of a velocity-non-conditioned model. We point out that looking at the bias from the NSE simulations, care should be taken in considering that we do not have the same number of particle in different cells; i.e. the bias coefficient should be divided with a different number of particles depending on the cell size. Comparing IECM simulation with SE and without SE we can see that there is a reduction of the bias in the smaller cell (about six times smaller) while the reduction is less evident in the larger cell (about two times smaller).

Fig. 11 shows the time-averaged scalar standard deviation $\sigma_\phi = (\overline{\phi^2} - \overline{\phi}^2)^{1/2}$ as a function of $1/N_{\mathrm{p}}^{(i_c)}$. We can see that the bias of the variance is less dependent on the micro-mixing model used. Moreover, comparing IECM simulation with SE and without SE we can see that there is a very strong reduction of the bias in the smaller cell (about twenty times smaller) and in the larger cell (about five times smaller).

The discretization error, D_Q, comes from the discretization of computational (spatial and temporal) space. Although this code uses spatial discretization only for the computation of scalar field statistics, the use of a cell-centered algorithm on broad cells can influence the accuracy of the micro-mixing step, because the instantaneous scalar field relaxes to a mean concentration which is not sufficiently local in physical space. To better

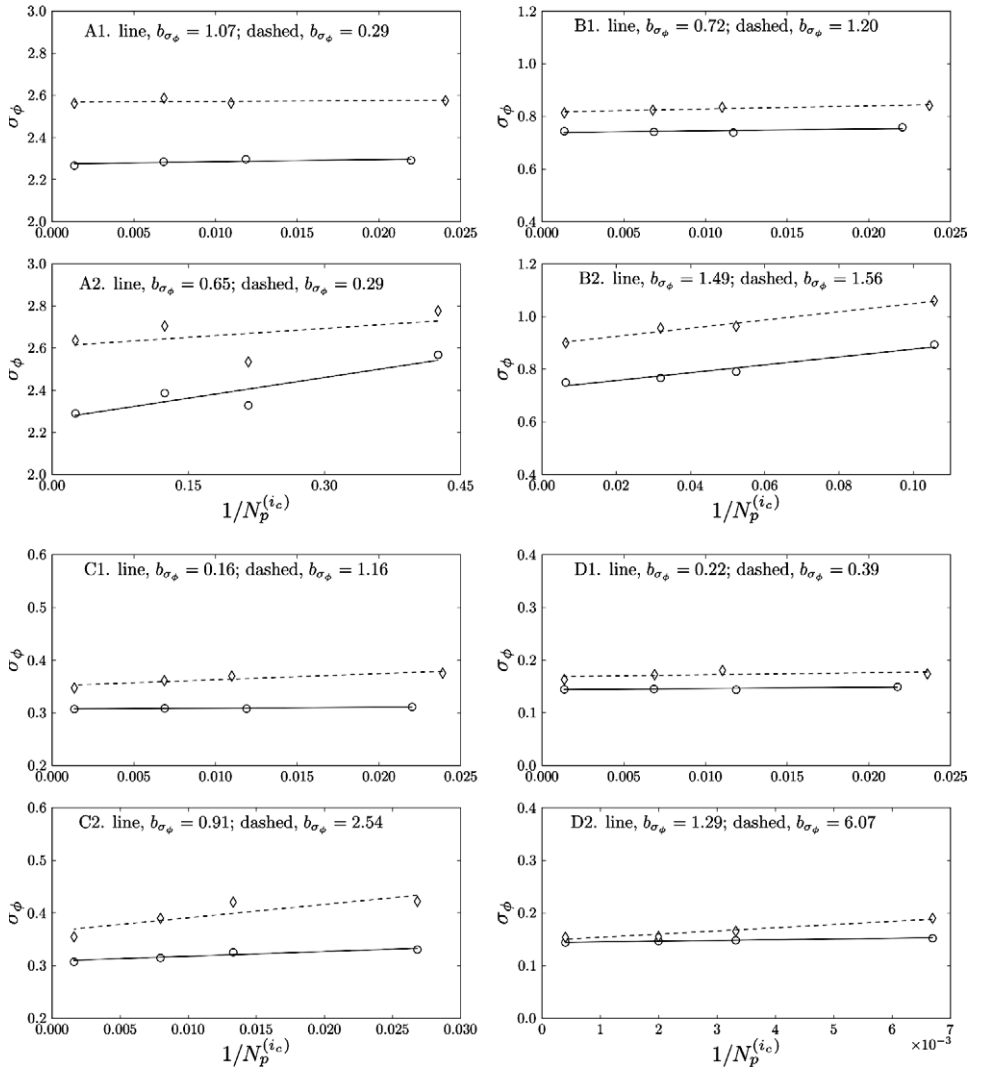

Fig. 11. As in Fig. 10, but for the scalar fluctuation, σ_ϕ. IEM (○) and IECM 9×9 (◇) results are shown with and without SE algorithm. Bias coefficient, b_{σ_ϕ}, is included at the top of plots. Measurement points are (0.46, 0.047: A), (0.6, 0.047: B), (0.8, 0.047: C) and (1.136, 0.047: D). Grid corresponds to setting 1.

isolate this effect, a constant value (0.1 s) for τ_m has been imposed throughout the domain. Fixing $N_p^{(i_c)}$ and varying cell dimensions can help to get a raw, but significant estimation of D_Q for IEM and IECM (9×9),

$$D_Q = d_Q(\Delta x \Delta y)^{1/2}/\sigma_y, \tag{35}$$

where d_Q is the slope of the line fits in Fig. 12. Fig. 12 shows $\overline{\phi}_{i_c}$ and σ_ϕ obtained from IEM and IECM 9×9 simulations for various grid setups. Grid setups are summarized in Table 2. Local grid dimensions are normalized on local plume mean depth σ_y, defined as

$$\sigma_y^2 = \int_0^\infty (y - \overline{y})^2 \overline{\phi}(y)\, \mathrm{d}y \Big/ \int_0^\infty \overline{\phi}(y)\, \mathrm{d}y, \tag{36}$$

where $\overline{y}$ is the mean plume height,

$$\overline{y} = \int_0^\infty y \overline{\phi}(y)\, \mathrm{d}y \Big/ \int_0^\infty \overline{\phi}(y)\, \mathrm{d}y. \tag{37}$$

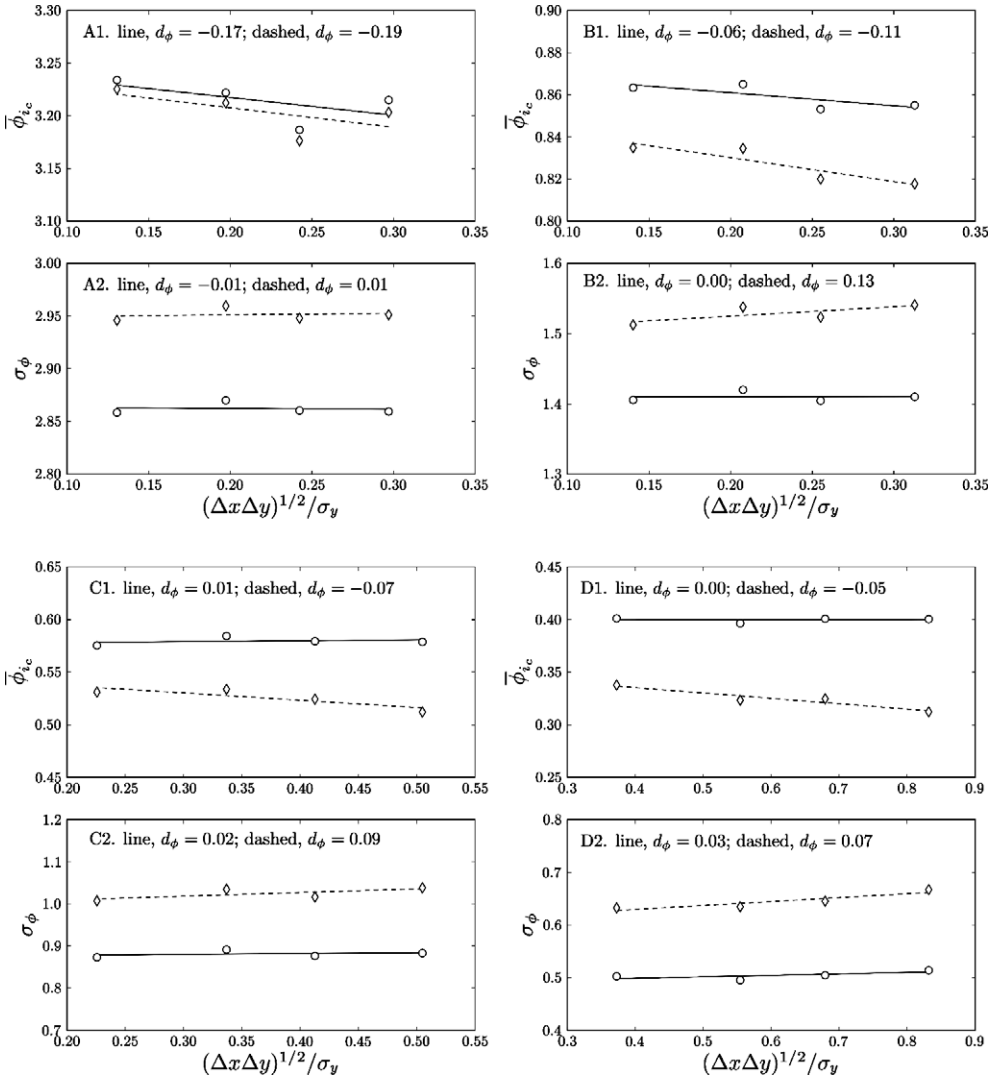

Fig. 12. Time-averaged concentration ($\overline{\phi}_{i_c}$) and standard deviation (σ_ϕ) plotted against local cell dimension ($(\Delta x \Delta y)^{1/2}$) normalized on local mean plume depth (σ_y), for both IEM (○) and IECM 9×9 (◇) mixing models. Spatial discretization coefficients d_ϕ and d_{σ_ϕ} are included at the top of plots. Measurement points are (0.46, 0.047: A), (0.6, 0.047: B), (0.8, 0.047: C) and (1.136, 0.047: D). $N_{\mathrm{p}}^{(i_c)} = 88$.

From Eq. (35) we can calculate a discretization error that remains in all the cases under 5%.

A better qualitative picture of the effects of grid variation is shown in Figs. 13 and 14. Here some vertical profiles of $\overline{\phi}_{i_c}$ and σ_ϕ are traced at different positions in the x direction, for different grid setups (see Table 2), both for IEM and IECM 9×9 models. What we can observe is the major sensitivity of IECM on $\Delta x \Delta y$ variations, in particular where cells are larger (i.e., plot D).

Also time discretization plays a relevant role in discretization error. In this work two discretization times have been introduced: the global time step ($\Delta t^{(\mathrm{g})}$) and the local time step ($\Delta t^{(\mathrm{loc})}$). $\Delta t^{(\mathrm{loc})}$ is the effective integration time of the differential equations (2)–(4). A major stability factor is given by the ratio between these two time scales. Fig. 15 shows that, within our range of variability of the parameters $\alpha^{(\mathrm{g})}$ and $\alpha^{(\mathrm{loc})}$, IECM 9×9 simulations give better results by increasing the ratio $\alpha^{(\mathrm{g})}/\alpha^{(\mathrm{loc})}$. This is due to the fact that, given $\Delta t^{(\mathrm{g})}$, a reduction in $\Delta^{(\mathrm{loc})}$ increases the probability that all velocity classes are visited by the particles, especially when low values of $N_{\mathrm{p}}^{(i_{\mathrm{vc}})}$ are used.

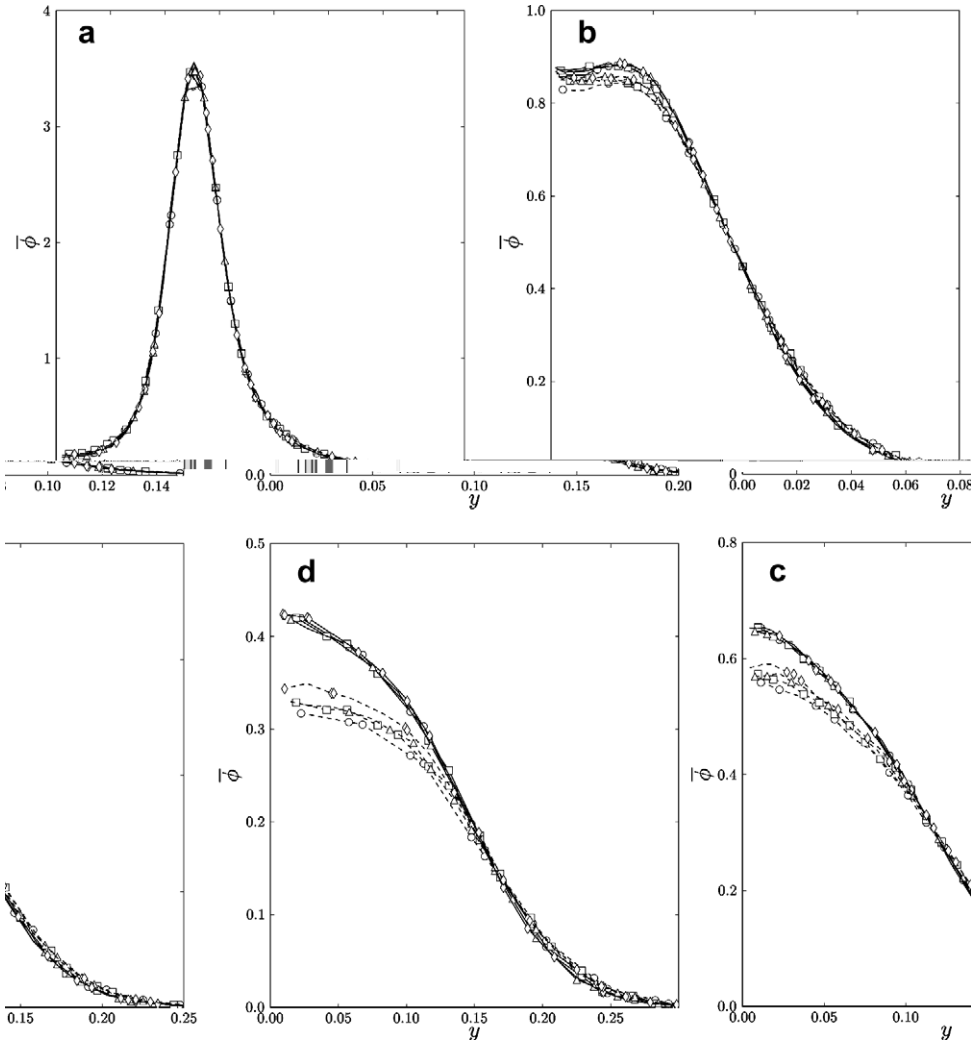

Fig. 13. Mean concentration vertical profiles, for IEM (continuous line) and IECM 9×9 (dashed line) micro-mixing models, obtained varying the local cells dimension. Measurement points are (0.46: a), (0.6: b), (0.8: c) and (1.136: d). Refer to Table 2 for grid settings details.

4.2. Micro-mixing model effects/choice

The choice of the micro-mixing model to use is not an easy task. In this section we compare the mean scalar fields obtained from using IEM and IECM models, maintaining fixed all the other simulation features. Firstly, we compare the mean concentration fields obtained using IEM and IECM (with different levels of discretization of the velocity) to the mean concentration obtained by a marked particle (MP), used as a reference. Secondly, we compare the concentration fluctuations field (σ_ϕ), between IEM and IECM using the IECM with 27×27 velocity classes as a reference.

We now briefly discuss the marked particle approach explaining why we are using this mean field as a reference. In the marked particle approach we do not use a micro-mixing model to compute the mean concentration field, $\langle \phi(x_i, t) \rangle$; this is obtained by releasing (instantaneously or continuously) a set of independent tracer particles from the source point and using the identity [29],

$$\langle \phi(x_i, t) \rangle = f_L(x_i, t | y_{i0}) \mathcal{Q}, \tag{38}$$

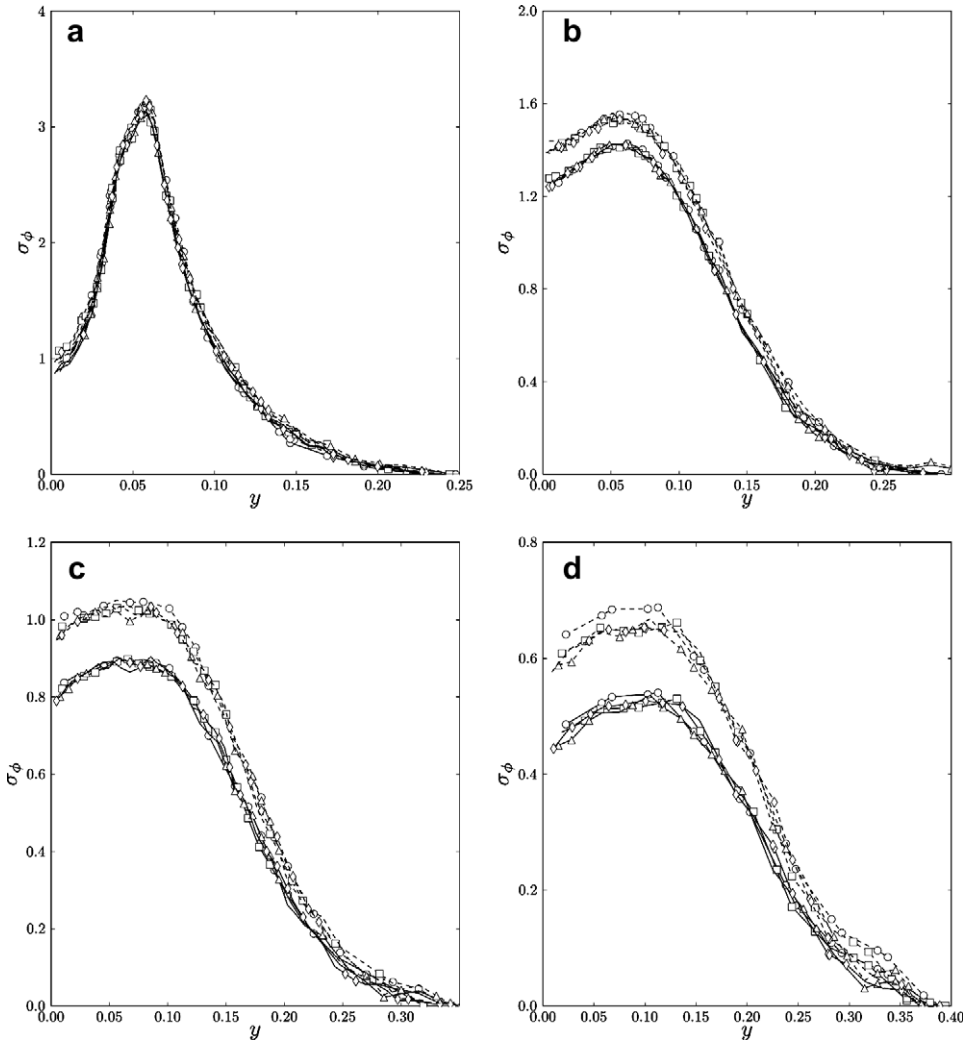

Fig. 14. As in Fig. 13 but for the scalar standard deviation, σ_ϕ. Refer to Table 2 for grid settings details. $N_{\mathrm{p}}^{(i_{\mathrm{c}})} = 88$.

where $f_{\mathrm{L}}(x_i, t|y_{i0})$ is the Lagrangian PDF for a particle starting at time t_0 from position y_{i0} to arrive at time t at position x_i; in this case y_{i0} represents the scalar source location. $\mathcal{Q}$ is the instantaneous mass of tracer released from the source.

The solution of Eqs. (2) and (3) for a set of independent particles starting from point y_{i0} at time t_0 corresponds to the solution of the FP equation for the Lagrangian joint PDF of velocity fluctuations and position, $f_{\mathrm{L}} = f_{\mathrm{L}}(v_i, x_i, t|v_{i0}, y_{i0})$,

$$\frac{\partial f_{\mathrm{L}}}{\partial t} + \frac{\partial (v_i + \langle U_i \rangle) f_{\mathrm{L}}}{\partial x_i} = -\frac{\partial a_i f_{\mathrm{L}}}{\partial v_i} + \frac{\partial^2 B_{ij} f_{\mathrm{L}}}{\partial v_i \partial v_j} - \frac{\partial \varphi_\alpha f_{\mathrm{L}}}{\partial \psi_\alpha}. \tag{39}$$

$f_{\mathrm{L}}(x_i, t|y_{i0})$ is related to f_{L} by the relationship

$$f_{\mathrm{L}}(x_i, t|y_{i0}) = \int\int f_{\mathrm{L}}(v_i, x_i, t|v_{i0}, y_{i0})\, \mathrm{d}u_i\, \mathrm{d}v_{i0}. \tag{40}$$

This approach allows one to obtain a mean scalar field directly from the dynamic equations, without using micro-mixing models, and to some extent we can say that the marked particle approach gives the exact estimation of $\langle \phi(x_i, t) \rangle$ for an assigned velocity PDF. Although very precise, this approach cannot provide moments of the scalar field higher than the first order and cannot handle directly a reactive scalar. This is the

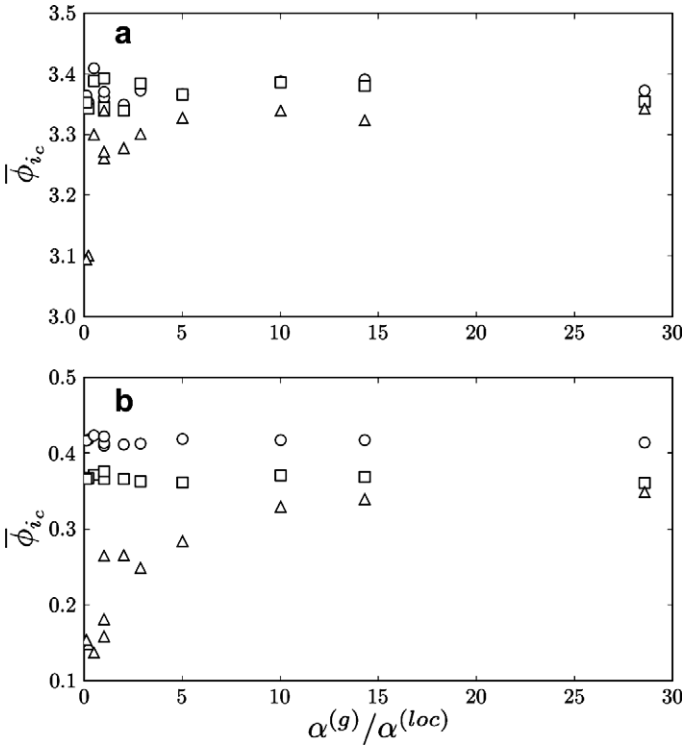

Fig. 15. Time-averaged concentration at locations (0.46, 0.047: a) and (1.136, 0.047: b) plotted against the ratio $\alpha^{(g)}/\alpha^{(loc)}$. Symbols are IEM (○), IECM 3×3 (□) and IECM 9×9 (△). The number of particles per cell in each simulation is $N_p^{(i_c)} = 88$.

reason for which we need the PDF micro-mixing modelling. For the same reason we will use the highly resolved (in velocity space) IECM as a reference during the comparison of the scalar fluctuation.

Figs. 16–18 show the comparison between the scalar field obtained by PDF modelling against that obtained by marked particle modelling. Fig. 16 is a scatter plot of $\overline{\phi}_{i_c}$ for IEM model with $N_p = 10^6$ and IECM with 3×3 velocity classes and 10^6 particles against the marked particle simulation. The plot on the right is a zoom

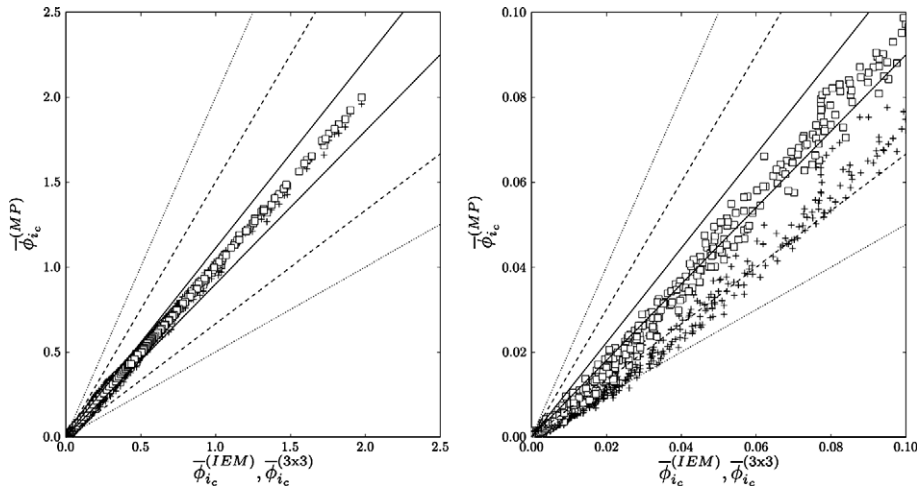

Fig. 16. Scatter plot of the time-averaged concentration ($\overline{\phi}_{i_c}$) for IEM (+) and IECM 3×3 (□) against marked particle model (MP), using $N_p = 10^6$ total particles. Lines are: continuous 10%, dashed 50% and dotted 100% differences. Right figure is a zoom of the left figure. Grid corresponds to setting 2.

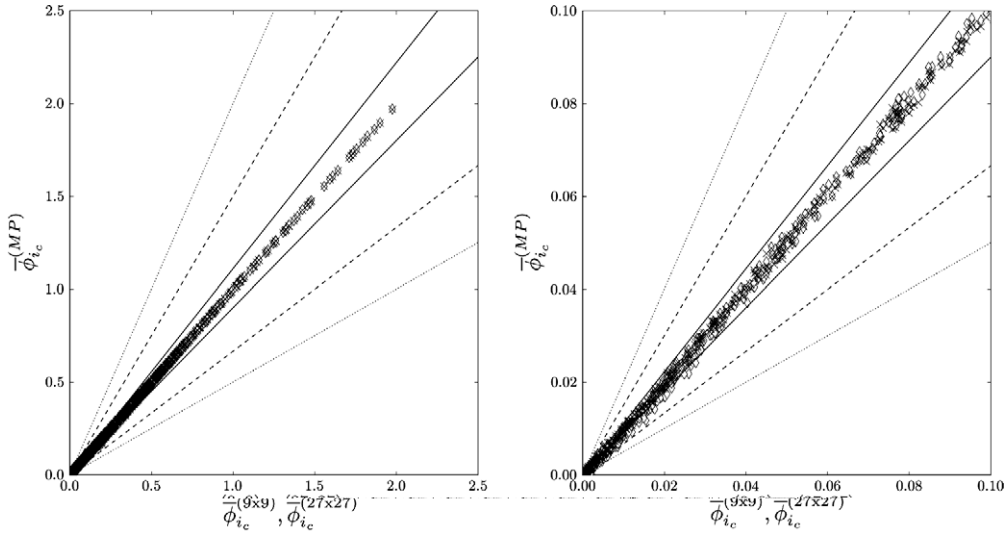

Fig. 17. Scatter plot of the time-averaged concentrations ($\overline{\phi}_{i_c}$) for IECM 9×9 ($\diamond$) and 27×27 ($\times$) against marked particle model (MP), using $N_p = 10^6$ total particles. Lines are: continuous 10%, dashed 50% and dotted 100% differences. Right figure is a zoom of the left figure. Grid corresponds to setting 2.

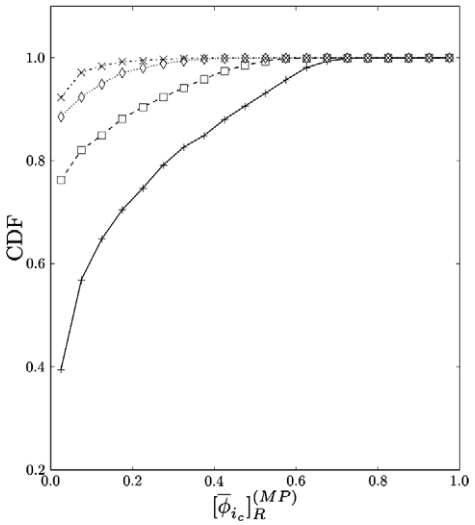

Fig. 18. Cumulative distribution function (CDF) of mean concentration relative error, $[\overline{\phi}_{i_c}]_R^{(MP)}$ for IEM (+), IECM with 3×3, 9×9 and 27×27 velocity classes ($\square$, $\diamond$ and $\times$) against marked particle model.

of the plot on left. Here we can see the distortion created by the IEM model since it does not respect the constraint (i) explained in Section 2.2. The improvement obtained using only three velocity classes is surprising and it will be better quantified. In general these scatter plots show that the differences between the mean reference field and that obtained by the IEM model increase with the distance from the source since the micromixing model acts for a longer time.

Fig. 17 shows the same comparison but for the IECM with 9×9 and 27×27 velocity classes ($N_p = 10^6$). It is easy to see the great improvement obtained with respect to the results of IEM and IECM 3×3 by increasing the number of velocity classes (an IEM can be seen as an IECM with only one velocity class). There are only minor differences between IECM 9×9 and 27×27 as we can see from Fig. 17.

A more quantitative comparison is given in Fig. 18; for each simulation is shown the cumulative density function (CDF) of relative differences,

$$[\overline{\phi}_{i_c}]_R^{(MP)} = \mathrm{abs}(\overline{\phi}_{i_c} - \overline{\phi}_{i_c}^{(MP)})/\overline{\phi}_{i_c}^{(MP)}. \tag{41}$$

The plot tells us that with the IEM model we have almost 100% of probability to obtain a result with relative difference under 80% and only 40% of probability to have a relative error below 5%. For IECM with 27×27 velocity classes the relative errors are with almost 100% probability under 20%. What is surprising is the great improvement of IECM 3×3 with respect to IEM; we have almost 80% of probability to have a relative error below 5%. The improvement obtained from 27×27 in comparison with 9×9 is not significant, if we consider the increase in computational requirements by increasing the number of velocity classes.

Figs. 19–21 show the comparison between the fluctuations of the scalar field obtained by IEM and IECM modelling with 3×3 and 9×9 velocity classes against IECM modelling with 27×27 velocity classes. IEM

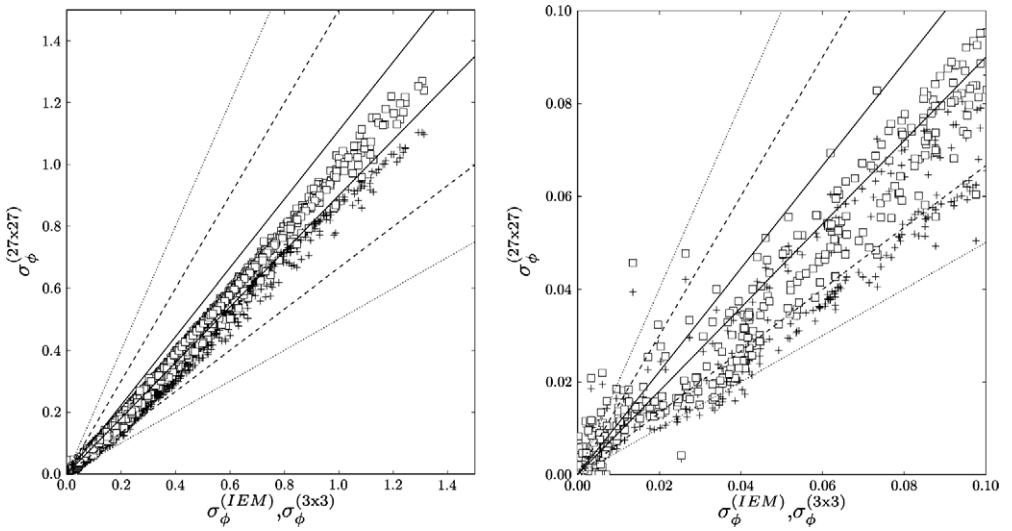

Fig. 19. Scatter plot of the time-averaged scalar variance (σ_ϕ) for IEM (+) and IECM 3×3 (□) against IECM 27×27 simulation, using $N_p = 10^6$ total particles. Lines are: continuous 10%, dashed 50% and dotted 100% differences. Right figure is a zoom of the left figure. Grid corresponds to setting 2.

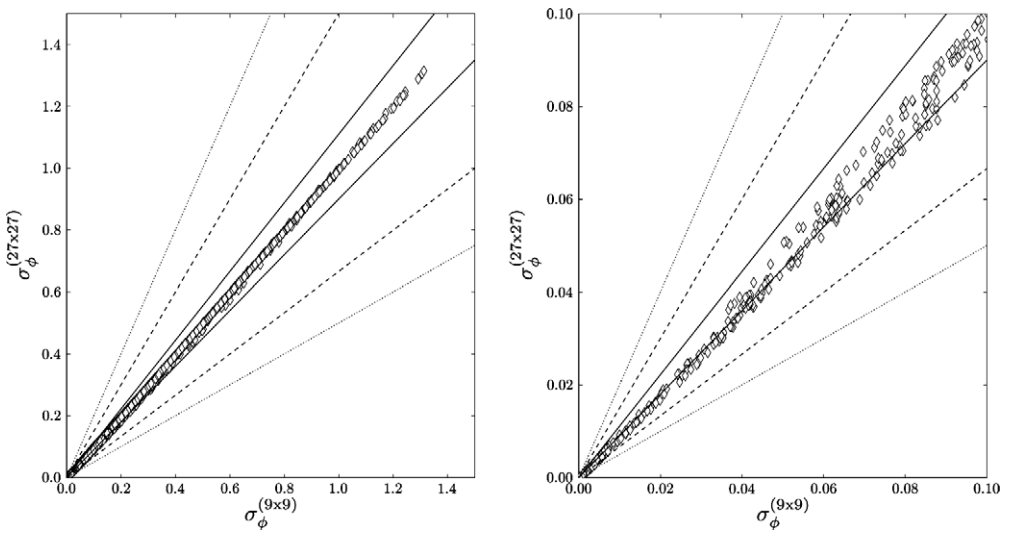

Fig. 20. Scatter plot of the time-averaged scalar variance (σ_ϕ) for IECM 9×9 (◇) against IECM 27×27 simulation, using $N_p = 10^6$ total particles. Lines are: continuous 10%, dashed 50% and dotted 100% differences. Right figure is a zoom of the left figure. Grid corresponds to setting 2.

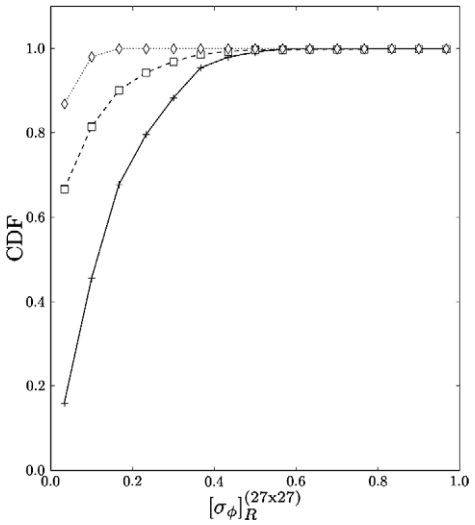

Fig. 21. Cumulative distribution function (CDF) of scalar variance relative error, $[\sigma_\phi]_{\mathrm{R}}^{(27\times27)}$ for IEM (+), IECM with 3×3 and 9×9 velocity classes (□ and ◇) against IECM with 27×27 velocity classes.

brings poor results. The IEM 3×3 give again a good improvement especially for higher values of σ_ϕ. IECM with 9×9 classes is in good accordance with reference simulation results, as we can also see in Fig. 21, where CDFs of relative difference

$$[\sigma_\phi]_{\mathrm{R}}^{(27\times27)} = \mathrm{abs}(\sigma_\phi - \sigma_\phi^{(27\times27)})/\sigma_\phi^{(27\times27)} \tag{42}$$

are presented. This comparison is somewhat less rigorous than that with the marked particle model since there is a dependence from the micro-mixing time scale, i.e. the time scale could be modified to give a better agreement for the IEM model. However, the improvement would be only apparent since actually the intensity of concentration fluctuations (the ratio of the rms and the mean) would be different.

5. Conclusion

A probability density function (PDF) code for the study of atmospheric scalar dispersion from small sources has been developed. This is based on a Monte Carlo algorithm in which model fluid particles are moved in a block-structured grid using [40] well-mixed criteria and adopting a splitting/erasing procedure that preserves a constant number of particles in every cell. This algorithm allows to refine the computational grid in near-source regions thus accounting for sharp scalar gradients and optimizing computational resources.

The numerical analysis of this PDF/Monte Carlo code emphasizes the benefits introduced by the algorithm, in particular, underlining the effective reduction of the numerical errors (statistical and bias) introduced by the splitting/erasing procedure.

A fundamental part in every PDF simulations of scalar dispersion is the micro-mixing model which defines the rate of decay of scalar fluctuations. A comparison between interaction by exchange with the mean (IEM) and interaction by exchange with the conditional mean (IECM) micro-mixing models has been achieved, showing the superiority of the IECM model with respect to IEM when the mean concentration field calculated from a marked particle simulation is used as a reference. In particular, the IECM model introduces effective improvements in evaluating statistics of the scalar field even using only 3×3 velocity classes. The IECM model has shown a major sensitivity on simulation parameters (i.e., number of particles per cell, time step size, cell dimension) by showing a bigger level of bias if compared to IEM model results; this is primarily due to the need of also distributing particles in velocity space.

Although numerical analysis is presented for a two-dimensional situation, extension to three-dimensions is straightforward.

Acknowledgments

M. Cassiani and J. Albertson were supported by the office of Science (BER), US Department of Energy, and through the Southeast Regional Center of the National Institute for Global Environmental Change under Cooperative Agreement No. DE-FC02-03ER63613.

Appendix A. Drift coefficient

The drift coefficient, a_i, introduced in Eq. (3) is obtained following Thomson [40] for the well-mixed condition to be satisfied it is sufficient that the modelled PDF for the Eulerian velocity fluctuation, $f_u^* = f^*(u_i, x_i, t)$, satisfies Eq. (5). If we assume a Gaussian shape for f_u^*,

$$f_u^* = (2\pi)^{-3/2}(\det \tau_{ij})^{-1/2} \exp\left[-\frac{1}{2} u_i \tau_{ij}^{-1} u_j\right], \tag{A.1}$$

satisfying the Fokker–Planck equation (5), then the well mixed condition is

$$a_i f_u^* = \frac{\partial}{\partial x_k}\left(\frac{1}{2} b_{ij} b_{jk} f_u^*\right) + \Theta_i(\boldsymbol{u}, \boldsymbol{x}, t), \tag{A.2}$$

and following Sawford [35]

$$\frac{\partial \Theta_i}{\partial u_i} = -\frac{\partial f_u^*}{\partial t} - \frac{\partial}{\partial x_i}[(u_i + \langle U_i \rangle) f_u^*], \tag{A.3}$$

with $\Theta \to 0$ as $|\boldsymbol{u}| \to \infty$. Given $\langle b_{ij} b_{jk} \rangle = \delta_{ij} C_0 \varepsilon$, the Thomson's solution for the drift coefficient is

$$a_i = -\left(\frac{C_0 \varepsilon}{2}\right) \lambda_{ik} u_k + \frac{\Theta_i}{f_u^*}, \tag{A.4}$$

where the first term on RHS is the fading memory term. The second is the drift correction term and is given by [35]

$$\frac{\Theta_i}{f_u^*} = \frac{1}{2}\frac{\partial \tau_{ij}}{\partial x_j} + \left[\frac{\lambda_{jm}}{2}\left(\frac{\partial \tau_{im}}{\partial t}\right)\right] u_j + \left[\frac{\lambda_{jm}}{2}\left(\langle U_k \rangle \frac{\partial \tau_{im}}{\partial x_k}\right)\right] u_j + \left[\frac{\lambda_{km}}{2}\frac{\partial \tau_{im}}{\partial x_j}\right] u_j u_k, \tag{A.5}$$

where $\lambda_{ij} = \tau_{ij}^{-1}$, and $\tau_{ij} = \langle u_i u_j \rangle$.

In two-dimensional cases (directions x_1 and x_2), assuming horizontal homogeneity ($\partial/\partial x_1 = 0$), stationarity and that $U_2 = 0$ the two components of a_i become

$$a_1 = -\frac{C_0 \varepsilon}{2}(\lambda_{11} u_1 + \lambda_{12} u_2) + \frac{1}{2}\frac{\partial \tau_{12}}{\partial x_2} + \left(\frac{\lambda_{11}}{2}\frac{\partial \tau_{11}}{\partial x_2}\right) u_2 u_1 + \left(\frac{\lambda_{12}}{2}\frac{\partial \tau_{12}}{\partial x_2}\right) u_2 u_1 + \left(\frac{\lambda_{22}}{2}\frac{\partial \tau_{12}}{\partial x_2}\right) u_2^2 + \left(\frac{\lambda_{12}}{2}\frac{\partial \tau_{11}}{\partial x_2}\right) u_2^2, \tag{A.6}$$

and

$$a_2 = -\frac{C_0 \varepsilon}{2}(\lambda_{12} u_1 + \lambda_{22} u_2) + \frac{1}{2}\frac{\partial \tau_{22}}{\partial x_2} + \left(\frac{\lambda_{11}}{2}\frac{\partial \tau_{12}}{\partial x_2}\right) u_2 u_1 + \left(\frac{\lambda_{12}}{2}\frac{\tau_{22}}{\partial x_2}\right) u_2 u_1 + \left(\frac{\lambda_{12}}{2}\frac{\partial \tau_{12}}{\partial x_2}\right) u_2^2 + \left(\frac{\lambda_{22}}{2}\frac{\partial \tau_{22}}{\partial x_2}\right) u_2^2. \tag{A.7}$$

Here

$$\lambda_{11} = (\tau_{11} - \tau_{12}^2/\tau_{22})^{-1}, \tag{A.8}$$

$$\lambda_{22} = (\tau_{22} - \tau_{12}^2/\tau_{11})^{-1}, \tag{A.9}$$

$$\lambda_{12} = (\tau_{12} - \tau_{11}\tau_{22}/\tau_{12})^{-1}. \tag{A.10}$$

Appendix B. Micro-mixing time calculation

We define the micro-mixing time scale as $\tau_m = \mu\tau_r = \mu\sigma_r/\sigma_{ur}$, where μ is an empirical constant, σ_r the instantaneous plume spread and σ_{ur} is the standard deviation of the relative velocity fluctuations, $\sigma_{ur} = \langle u_r^2 \rangle^{1/2}$. u_r represents the difference between a turbulent velocity component and the corresponding velocity component of the instantaneous center of mass of a cluster of particles (see e.g. [12]).

σ_{ur} is modelled using the following formulation [11], strictly correct only in the inertial subrange,

$$\sigma_{ur}^2 = \sigma^2 \left(\frac{\sigma_r}{L}\right)^{2/3}, \tag{B.1}$$

where σ^2 define a locally averaged velocity variance $\sigma^2 = 2e/3 = (\sigma_u^2 + \sigma_v^2 + \sigma_u\sigma_v)/3$, where e is defined for the canopy layer using [1]. $L = (3\sigma^2/2)^{3/2}/\varepsilon$ is a characteristic length scale of the most energetic eddies. From Eq. (B.1), when $\sigma_r = L$ all the energy contributes to the plume expansion, and when $\sigma_r > L$ the constraint $\sigma_{ur} = \sigma$ is imposed.

σ_r is parametrized as

$$\sigma_r^2 = \frac{d_r^2}{1 + (d_r^2 - \sigma_0^2)/(\sigma_0^2 + 2\sigma^2 T_L t)}, \tag{B.2}$$

where the relative expansion is discretized as

$$d_r^2(t + \Delta t) = d_r^2(t) + 3C_r\varepsilon(t_0 + t)^2\Delta t, \tag{B.3}$$

with the condition $d_r^2(0) = \sigma_0^2$, where σ_0^2 is the size of the scalar source, C_r the Richardson–Obukhov constant and $T_L = 2\sigma^2/C_0\varepsilon$ the Lagrangian integral time scale. The upper boundary for τ_m is fixed to its default value $2e/(C_\phi\varepsilon)$, where C_ϕ is an empirical constant. The constants value that give a satisfactory agreement with the experimental data of [19] are: $C_0 = 2$, $\mu = 0.8$, $C_r = 0.1$, $C_\phi = 2$. We note that better parameterization for τ_r and therefore τ_m could be obtained following the approach proposed by [12].

All these quantities are calculated at the particle location, obtaining a position dependent τ_m.

Inside the code, τ_m is calculated during a pre-processing step, using a small ensemble of particles (1×10^5) released instantaneously at the source location. From this first step a cell-centered mean τ_m is calculated and then used during the remaining of the simulation. In regions of the domain not reached by the pre-processing particles τ_m is assumed to be $2e/(C_\phi\varepsilon)$.

Appendix C. Velocity conditioning and coordinate transformation

In concentration field estimation the IECM needs the conditioning on physical and velocity space. This implies that particles interact with those located in the same physical-velocity-cell. This means that in 2D computation we need to estimate the mean concentration field in a 4D space (x, y, u, v)-space. The more this space is discretized the more the estimation is precise (given an appropriate number of particles per 4D cell). The velocity space is divided in equally probable cells; that is, given a standard deviation (σ_u, σ_v) for the velocity fluctuations (u, v), the cell dimension is defined under the normalized velocity PDF so that the cells contain the same probability to occur.

In many cases the velocity components are correlated; therefore, to simplify the creation of the cells in velocity space it is better to define a new coordinate system for the velocity PDF.

In this context we define the following correlation angle, γ,

$$\tan 2\gamma = \frac{2\langle uv \rangle}{\sigma_u^2 - \sigma_v^2}, \tag{C.1}$$

which defines principal axes of the velocity space,

$$\xi = u\cos\gamma + \eta\sin\gamma, \tag{C.2}$$

$$\eta = -u\sin\gamma + v\cos\gamma. \tag{C.3}$$

and consequently

$$\sigma_\xi^2 = \sigma_u^2 \cos^2\gamma + \sigma_v^2 \sin^2\gamma + 2\langle uv\rangle \sin\gamma\cos\gamma, \tag{C.4}$$

$$\sigma_\eta^2 = \sigma_u^2 \sin^2\gamma + \sigma_v^2 \cos^2\gamma - 2\langle uv\rangle \sin\gamma\cos\gamma, \tag{C.5}$$

which represents the standard deviations for the transformed velocity space, (ξ, η), PDF.

References

[1] Y. Brunet, J.J. Finnigan, M.R. Raupach, A wind tunnel study of air flow in waving wheat: single-point velocity statistics, Boundary Layer Meteorol. 70 (1994) 95–132.
[2] M. Cassiani, P. Franzese, U. Giostra, A PDF micromixing model of dispersion for atmospheric flow. Part I: development of the model, application to homogeneous turbulence and to neutral boundary layer, Atmos. Environ. 39 (8) (2005) 1457–1469.
[3] M. Cassiani, P. Franzese, U. Giostra, A PDF micromixing model of dispersion for atmospheric flow. Part II: application to a convective boundary layer, Atmos. Environ. 39 (8) (2005) 1457–1469.
[4] M. Cassiani, A. Radicchi, U. Giostra, Probability density function modelling of concentration in and above a canopy layer, Agric. Forest Meterol. 133 (2005) 153–165.
[5] M. Cassiani, A. Radicchi, J.D. Albertson, Modeling of concentration PDF in canopy generated turbulence, Boundary Layer Meteorol. (in press), doi:10.1007/510546-006-9122-0.
[6] P.C. Chatwin, Singular PDFs of a dispersing scalar in turbulence, Flow Turbul. Combust. 72 (2004) 273–285.
[7] C. Dopazo, L. Valino, F. Fuego, Statistical description of the turbulent mixing of scalar fields, Int. J. Mod. Phys. B 11 (25) (1997).
[8] T.K. Flesch, J.D. Wilson, A two dimensional trajectory simulation model for non Gaussian inhomogeneous turbulence within plant canopies, Boundary Layer Meteorol. 61 (1992) 349–374.
[9] R.O. Fox, On velocity conditioned scalar mixing in homogeneous turbulence, Phys. Fluids 8 (1996) 2678–2891.
[10] R.O. Fox, Computational Models for Turbulent Reacting Flows, Cambridge University Press, Cambridge, 2003.
[11] P. Franzese, Lagrangian stochastic modelling of a fluctuating plume in the convective boundary layer, Atmos. Environ. 37 (2003) 1691–1701.
[12] P. Franzese, M. Cassiani, A statistical theory of turbulent relative dispersion, J. Fluid Mech. (accepted), doi:10.1017/5002211-200-6003375.
[13] C.W. Gardiner, Handbook of Stochastic Methods for Physics Chemistry and the Natural Sciences, Springer, Berlin, 1983.
[14] M. Gonzalez, Analysis of the effect of microscale turbulence on atmospheric chemical reactions by means of the PDF approach, Atmos. Environ. 31 (1997) 575–586.
[15] P. Jenny, S.B. Pope, M. Muradoglu, D.A. Caughey, A hybrid algorithm for the joint PDF equation of turbulent reactive flows, J. Comput. Phys. 166 (2001) 218–252.
[16] P.E. Kloeden, E. Platen, Numerical Solution of Stochastic Differential Equations, Springer, Berlin, 1992.
[17] A.K. Luhar, B.L. Sawford, Micro-mixing modelling of concentration fluctuations in inhomogeneous turbulence in the convective boundary layer, Boundary Layer Meteorol. 114 (2005) 1–30.
[18] G. Li, F. Modest, An effective particle tracing scheme on structured/unstructured grids in hybrid finite volume/PDF Monte Carlo methods, J. Comput. Phys. 173 (2001) 187–207.
[19] B.J. Legg, M.R. Raupach, P.A. Coppin, Experiments on scalar dispersion within a model plant canopy. Part III: an elevated line source, Boundary Layer Meteorol. 35 (1986) 277–302.
[20] T.S. Lundgren, Distribution functions in the statistical theory of turbulence, Phys. Fluids 10 (1967) 969–975.
[21] J.-P. Minier, E. Peirano, The pdf approach to turbulent polydispersed two-phase flows, Phys. Rep. 352 (2001) 1–214.
[22] M. Muradoglu, S.B. Pope, Local time-stepping algorithm for solving probability density function turbulence model equations, AIAA J. 40 (9) (2002) 1755–1763.
[23] A.M. Obukhov, Description of turbulence in terms of Lagrangian variables, Adv. Geophys. 6 (1959) 113–116.
[24] N. Peters, Turbulent Combustion, Cambridge University Press, Cambridge, 2000.
[25] D. Poggi, G. Katul, J. Albertson, Scalar dispersion within model canopy: measurement and three-dimensional Lagrangian models, Adv. Water Resour. 29 (2006) 326–335.
[26] S.B. Pope, PDF methods for turbulent reactive flows, Prog. Energy Combust. Sci. 11 (1985) 119–192.
[27] S.B. Pope, Consistency conditions for random-walk models of turbulent dispersion, Phys. Fluids 30 (8) (1987) 2374–2379.
[28] S.B. Pope, The vanishing effect of molecular diffusivity on turbulent dispersion: implications for turbulent mixing and the scalar flux, J. Fluid Mech. 359 (1998) 299–311.
[29] S.B. Pope, Turbulent Flows, Cambridge University Press, Cambridge, 2000.
[30] M.B. Priestley, Spectral Analysis and Time Series, Academic Press, New York, 1981.
[31] V. Raman, R.O. Fox, A.D. Harvey, Hybrid finite-volume/transported PDF simulations of a partially premixed methane-air flame, Combust. Flame 136 (2004) 327–350.
[32] M.R. Raupach, P.A. Coppin, B.J. Legg, Experiments on scalar dispersion within a model plant canopy. Part I: the turbulence structure, Boundary Layer Meteorol. 35 (1986) 21–52.
[33] Raupach, M.R., Coppin, P.A., Legg, B.J., Erratum to M.R. Raupach, P.A. Coppin, B.J. Legg, Experiments on scalar dispersion within a model plant canopy. Part I: the turbulence structure, Boundary Layer Meteorol. 35 (1986) 21–52; Boundary Layer Meteorol. 39 (1986) 423–424.

[35] B.L. Sawford, Rotation of trajectories in Lagrangian stochastic model of turbulent dispersion, Boundary-Layer Meteorology 93 (1999) 411–424.
[36] B.L. Sawford, Conditional scalar mixing statistics in homogeneous isotropic turbulence, New J. Phys. 6 (2004) 55.
[37] B.L. Sawford, Micro-mixing modelling of scalar fluctuations for plumes in homogeneous turbulence, Flow Turbul. Combust. 72 (2004) 133–160.
[38] S. Subramaniam, D.C. Haworth, A PDF method for turbulent mixing and combustion on three-dimensional unstructured deforming meshes, Int. J. Eng. Res. 1 (2000) 171–190.
[39] S. Subramaniam, S.B. Pope, A mixing model for turbulent reactive flows based on Euclidean minimum spanning trees, Combust. Flame 115 (1998) 487–514.
[40] D.J. Thomson, Criteria for the selection of stochastic models of particle trajectories in turbulent flows, J. Fluid Mech. 180 (1987) 529–556.
[41] J. Villermaux, J.C. Devillon, in: Proceedings of the Second International Symposium on Chemical Reaction Engineering, Elsevier, New York, 1972.
[42] J.D. Wilson, B.L. Sawford, Review of Lagrangian stochastic models of particle trajectories in the turbulent atmosphere, Boundary-Layer Meteorol. 78 (1996) 191–210.
[43] J. Xu, S.B. Pope, Assessment of numerical accuracy of PDF/Monte Carlo methods for turbulent reacting flows, J. Comput. Phys. 152 (1999) 192–230.